nature immunology

Article

https://doi.org/10.1038/s41590-025-02100-2

A critical role of N^4-acetylation of cytidine in mRNA by NAT10 in T cell expansion and antiviral immunity

Received: 11 February 2024

Accepted: 26 January 2025

Published online: 5 March 2025

Check for updates

Lu Sun[1,2,9], Xiaoyan Li[3,4,9], Feixiang Xu[5,9], Yuwen Chen[6], Xushuo Li[6], Zhicheng Yang[6], Ying Yang[6], Ke Wang[6], Tianyi Ren[7], Zihao Lin[6], Hua Wang[3], Xiangdong Wang[1], Yan Lu[8] ✉, Zhenju Song[1,5] ✉, Zhou-Li Cheng[6] ✉ & Duojiao Wu[1,6] ✉

Following activation, naive T cells exit quiescence and require global translation for rapid expansion, yet the underlying mechanisms remain unclear. Here, we show that during T cell activation, cells upregulate the expression of *N*-acetyltransferase 10 (NAT10), an enzyme responsible for N^4-acetylcytidine (ac^4C) modification of mRNAs. ac^4C-modified *Myc* mRNAs show higher translation efficiency, enabling rapid synthesis of MYC protein and supporting robust T cell expansion. Conditional deletion of *Nat10* in mouse T cells causes severe cell cycle arrest and limitation of cell expansion due to MYC deficiency, ultimately exacerbating infection in an acute lymphocytic choriomeningitis virus model. Additionally, T cells from older individuals with lower NAT10 levels show proliferative defects, which may partially account for impaired antiviral responses in older individuals. This study reveals a mechanism governing T cell expansion, signal-dependent mRNA degradation induction and the potential in vivo biological significance of ac^4C modification in T cell-mediated immune responses.

As a key component of the immune system, naive T (T_N) cells undergo rapid clonal expansion and differentiation following antigen stimulation to execute an efficient immune response. During this process, T cells reprogram the proteome and substantially augment protein synthesis to fulfill robust bioenergetic and biosynthetic demands. A study of the ribosomal translation dynamics of T cells showed that in the initial phases of T cell activation (6 h after T cell antigen receptor (TCR) stimulation), protein synthesis can increase to as much as five times that of the resting state, whereas cellular RNA content increases by only 1.37 times, indicating the core role of post-transcriptional regulation at this stage[1].

Unraveling the mechanisms underpinning cell expansion is pivotal for understanding the regulation of immune responses and gaining insights into immune dysfunction.

Currently, over 170 ribonucleotide modifications have been identified, with new types continually emerging. Following RNA synthesis, a wide variety of molecular changes could be implemented by highly conserved enzyme systems under physiological or

[1]Shanghai Key Laboratory of Lung Inflammation and Injury, Zhongshan Hospital, Fudan University, Shanghai, China. [2]Department of Medical Oncology, Shanghai Cancer Center & Department of Oncology, Shanghai Medical College, Fudan University, Shanghai, China. [3]Department of Oncology, The First Affiliated Hospital of Anhui Medical University, Hefei, China. [4]Department of Geriatrics, Xinhua Hospital, Shanghai Jiaotong University School of Medicine, Shanghai, China. [5]Department of Emergency Medicine, Zhongshan Hospital, Fudan University, Shanghai, China. [6]Jinshan Hospital Center for Tumor Diagnosis & Therapy, Jinshan Hospital, Fudan University, Shanghai, China. [7]Department of Gastroenterology, Xinhua Hospital, Shanghai Jiao Tong University School of Medicine, Shanghai, China. [8]Institute of Metabolism and Regenerative Medicine, Digestive Endoscopic Center, Shanghai Sixth People's Hospital, Shanghai Jiao Tong University School of Medicine, Shanghai, China. [9]These authors contributed equally: Lu Sun, Xiaoyan Li, Feixiang Xu. ✉e-mail: luyan5011@shsmu.edu.cn; song.zhenju@zs-hospital.sh.cn; chengzhouli@fudan.edu.cn; wu.duojiao@zs-hospital.sh.cn

pathological circumstances. N^4-Acetylcytidine (ac^4C) is currently the only acetylation mark observed in RNA. In 2018, Arango et al. reported the 'writer' protein for ac^4C, *N*-acetyltransferase 10 (NAT10), as well as the biological function of ac^4C in maintaining mRNA stability and promoting translation efficacy. The potential role of NAT10-mediated ac^4C modification in several diseases and conditions, such as premature aging, autoimmune diseases, infection, inflammation and cancer, has been reported[2–6].

Recent studies have revealed the epitranscriptomic mechanisms in T cell homeostasis adaptation. N^6-Methyladenosine modification of mRNAs can promote T cell proliferation and differentiation via accelerating the degradation of suppressors of cytokine signaling family genes, which encode major physiological inhibitors of JAK–STAT signaling pathways[7]. Epitranscriptomic regulation of T cell functionality has increasingly become a research hot spot, but the physiological role of ac^4C in mammalian T cells is still unknown.

Here, we investigated how ac^4C controls T cell homeostasis via conditional knockout (CKO) of *Nat10*. Our data indicated that loss of NAT10 significantly diminished ac^4C marks on mRNAs, which in turn changed the entire transcriptional profile of T cells. As a result, CKO mice showed significant defective T cell expansion, which aggravated infection in a mouse lymphocytic choriomeningitis virus (LCMV) model. From a mechanistic standpoint, the installation of mRNA-ac^4C by NAT10 on early upregulated mRNAs contributed to the translation of key proteins essential for T cell proliferation, notably MYC. MYC, in turn, propeled T cells into mitosis, enabling them to complete the cell cycle. Notably, the NAT10–MYC axis displayed a certain level of impairment in T cells derived from older individuals, which may partially account for age-related antiviral defects in this population. Together, these findings highlight the role of mRNA-ac^4C modification as a translational checkpoint of T cell expansion mainly via facilitating MYC protein synthesis.

Results

NAT10 is upregulated during T cell activation

To investigate the potential role of NAT10 in T cell functionality, we first analyzed the dynamic changes in NAT10 expression in T cells undergoing TCR-based activation. We found that, compared to the low expression of NAT10 in mouse splenic T_N cells, cells treated with anti-CD3/CD28 for 6, 24 and 48 h showed dramatic increases in NAT10 protein expression (Fig. 1a). Consistently, dot blots demonstrated enhanced ac^4C abundance on total RNA isolated from activated T cells, with methylene blue staining as a loading control (Fig. 1b). Next, to determine whether NAT10 is also involved in T cell activation in vivo, we developed an acute infection mouse model using LCMV (Fig. 1c). Wild-type (WT) mice were intraperitoneally infected with 2×10^5 plaque-forming units (p.f.u.) of LCMV Armstrong and killed at 2, 4, 6, 8, 12 and 16 days after infection[8]. Serum was collected for RNA extraction, and $CD3^+$ T cells were isolated for western blotting. LCMV titers measured by quantitative PCR (qPCR) showed that LCMV replicated rapidly at early stages of infection, and this was essentially eliminated at day 8 (Fig. 1d). The dynamic changes in NAT10 protein expression were aligned to viral load, suggesting that, similar to in vitro T cell activation (Fig. 1a), NAT10 in T cells also responds to activation and viral clearance in vivo (Fig. 1e).

We then sought to determine the potential upstream signaling responsible for NAT10 upregulation during T cell activation. As TCR, interleukin-2 (IL-2) and IL-7 signaling serve as the major pathways at the early stage of T cell activation, we stimulated T_N cells with TCR (anti-CD3/CD28), IL-2 and IL-7 for the indicated lengths of time, respectively (Fig. 1f,g). Given NAT10's specific response to anti-CD3/CD28 stimulation, it might be downstream of TCR signaling (Fig. 1g). We then reanalyzed the published activated T cell chromatin immunoprecipitation with sequencing (ChIP–seq) data to explore the probable binding sites of the major transcription factors within TCR pathways (Fig. 1h)[9–12]. c-JUN, NFAT2 and P65 were found bound within the *Nat10* body or 2 kb upstream, suggesting their potential roles in regulating *Nat10* transcription (Fig. 1h). We then stimulated T_N cells with anti-CD3/CD28 for 24 h, together with inhibitors of these transcription factors, and found that only the c-JUN inhibitor led to decreased NAT10 expression in a dose-dependent manner (Fig. 1i). Consistently, qPCR analysis under the same condition showed a significant drop in *Nat10* transcript levels following c-JUN inhibition (Fig. 1j). Furthermore, western blot analysis revealed an upward trend in c-JUN expression during T cell activation, similar to but before that of NAT10 (Fig. 1g). Finally, the binding of c-JUN to the *Nat10* locus was confirmed by ChIP–qPCR experiments (Fig. 1k). Together, these data suggest that TCR signaling activates NAT10-mediated ac^4C processing during T cell activation via c-JUN.

NAT10 helps to maintain the pool of T cells

To further explore the specific role of NAT10 in T cells, we generated *Nat10* T cell-CKO ($Nat10^{fl/fl}Cd4^{Cre}$; hereafter CKO) mice using a Cre/*loxP* recombination system. CKO T cells exhibited diminished NAT10 expression and ac^4C levels compared to those from $Nat10^{fl/fl}$ (hereafter FLOX) mice (Fig. 2a,b). Single-cell RNA sequencing (scRNA-seq) was then conducted on thymic and splenic cells from 6- to 8-week-old FLOX and CKO mice to depict NAT10's role in T cell development and differentiation. In total, eight cell types, including 28 clusters, were revealed via unsupervised hierarchical clustering and visualized by *t*-distributed stochastic neighbor embedding (t-SNE; Fig. 2c and Extended Data Fig. 1a). The scRNA-seq data showed that T cells were significantly reduced in the spleen but not in the thymus, indicating that CKO of *Nat10* mainly perturbed splenic rather than thymic T cell development (Fig. 2d,e and Extended Data Fig. 1b). Next, we extracted splenic T cells for deeper uniform manifold approximation and projection (UMAP) dimension reduction analysis. A total of eight T cell clusters were presented according to known marker genes, and all these populations were decreased in CKO mice (Extended Data Fig. 1c,d). Consistent with the scRNA-seq data, flow cytometry (FCM) analysis also confirmed dramatic shrinkage of the CKO T cell pool (Fig. 2f–i). These changes were extensive in not only immune organs but also other parenchymal organs, such as the lung and kidney (Fig. 2j). However, no changes were detected between FLOX and CKO T cells of the thymus in the double-negative, double-positive and mature single-positive stages, respectively (Fig. 2k), indicating that the early developmental stages of T cells in the thymus are unaffected. In addition to cell proportions, differentially expressed genes were also analyzed. Compared to controls (blue block), the top eight upregulated (*Gh*, *Ttn*, *Smu1*, *Top2a*, *Igfbp4*, *Tnfsf8*, *Cd7* and *Bcl2*) and top ten downregulated (*Rps7*, *Rps28*, *Rps24*, *Rps9*, *Rps16*, *Icos*, *Rps28*, *Rpl12*, *Cd8a* and *Cd8b1*) genes in CKO T cells were assessed (Extended Data Fig. 1e). We found that genes encoding ribosomal proteins were dramatically decreased in expression following NAT10 deficiency, which is consistent with earlier reports[13–15]. Notably, the critical T cell markers *CD8a* and *CD8b1* were also considerably downregulated in $CD8^+$ CKO T cells at both the mRNA and protein levels, which partially accounts for the contraction of $CD3^+$, especially $CD8^+$, T cells (Extended Data Fig. 1f).

Functionally, CKO T cells were more hyperactive than FLOX control T cells. The fraction of T_N cells decreased, whereas the effector T (T_{EFF}) cell proportion increased in CKO T cells in the resting state (Extended Data Fig. 2a). CD69 and CD44, T cell early activation markers, were more highly expressed in CKO T cells following TCR stimulation (Extended Data Fig. 2b). Additionally, without stimulation, CKO $CD8^+$ T cells synthesized more effector molecules under quiescent conditions, such as interferon-γ (IFNγ), granzyme A (GZMA), granzyme B (GZMB), tumor necrosis factor (TNF) and perforin (Extended Data Fig. 2c–g). However, the reason why T cells are hyperactive following NAT10 deficiency remains largely unknown. Lymphopenia-induced spontaneous proliferation may be involved in this phenotypic shift[16]. Dysregulation of key molecules that maintain cellular homeostasis may also contribute. The specific mechanism remains to be discovered.

https://doi.org/10.1038/s41590-025-02100-2

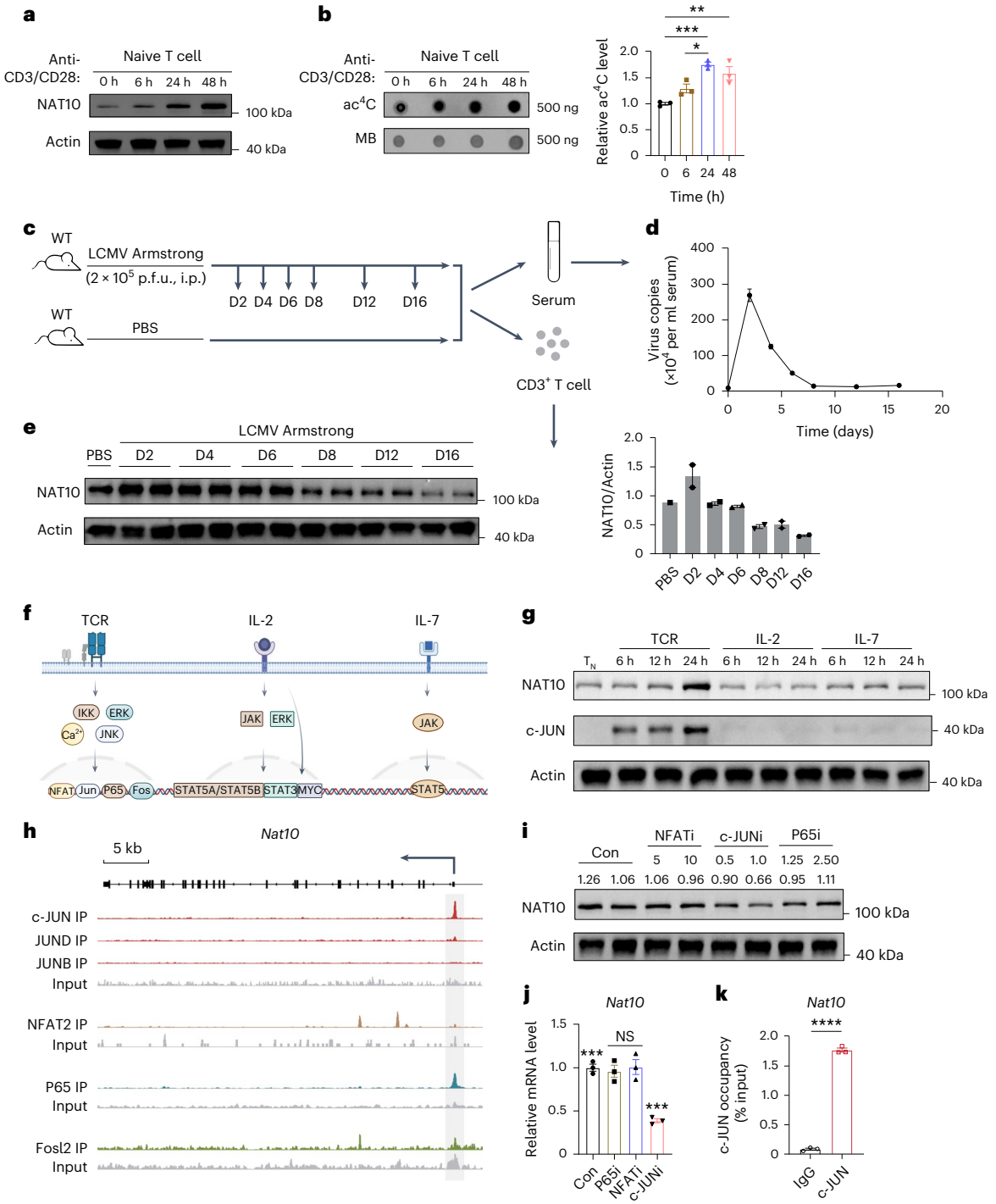

Fig. 1 | NAT10 is upregulated during T cell activation. a, NAT10 expression in $CD3^+$ T_N cells stimulated with anti-CD3/CD28 for the indicated lengths of time. **b**, Dot blot and densitometry analysis of ac^4C modifications in total RNA (500 ng) of $CD3^+$ T_N cells stimulated with anti-CD3/CD28 for the indicated lengths of time. Left, representative anti-ac^4C dot blot. Right, bar graph showing the relative ac^4C intensities normalized to total RNA quantified by methylene blue; $n = 3$; $^*P = 0.0153$, $^{**}P = 0.0039$ and $^{***}P = 0.0007$. **c**, Schematic of the acute LCMV infection model in WT mice. Eight-week-old WT mice were intraperitoneally injected with 2×10^5 p.f.u. LCMV (Armstrong strain) and killed at 2, 4, 6, 8, 12 and 16 days after infection. Mice treated with equal volumes of PBS served as controls. Serum RNA and $CD3^+$ T cells were isolated for further analysis; D, day; i.p., intraperitoneal. **d**, Changes in serum viral load during infection; $n = 3$. **e**, Western blot and densitometry analysis of NAT10 protein expression in T cells of LCMV Armstrong-infected mice at the indicated times. Each blot represents an independent biological sample. **f**, Schematic diagram of TCR, IL-2 and IL-7 signaling pathways during T cell activation. Image created using BioRender. **g**, NAT10 and c-JUN expression in $CD3^+$ T_N cells stimulated with TCR (anti-CD3/CD28), IL-2 and IL-7 for the indicated lengths of time. **h**, IGV snapshots showing c-JUN, JUND, JUNB, NFAT2, P65 and FOSL2 binding sites at the *Nat10* locus. The arrow indicates the start site and transcription direction. **i**, NAT10 expression in $CD3^+$ T_N cells stimulated with anti-CD3/CD28 for 24 h in the presence of NFAT inhibitor (NFATi), c-JUN inhibitor (c-JUNi), P65 inhibitor (P65i) and an equal volume of DMSO at the indicated concentrations (in μM), respectively. **j**, *Nat10* expression at the transcriptional level under the same conditions as in **i**; $n = 3$. The following are the exact P values from left to right: $^{***}P = 0.0004$, $^{***}P = 0.0007$, $^{***}P = 0.0004$ and not significant (NS), $P > 0.05$; Con, control. **k**, c-JUN ChIP–qPCR for the *Nat10* locus in $CD3^+$ T_N cells stimulated with anti-CD3/CD28 for 24 h; $n = 3$; $^{****}P < 0.0001$. n refers to the number of biologically independent samples. Error bars represent mean ± s.e.m. (**b**, **d**, **e**, **j** and **k**). Representative data of three independent experiments are presented (**a**, **b**, **d**, **e**, **g** and **i**). Data were analyzed by two-tailed, one-way analysis of variance (ANOVA) with Tukey's multiple comparisons test (**b** and **j**) and two-tailed, unpaired t-test (**k**).

https://doi.org/10.1038/s41590-025-02100-2

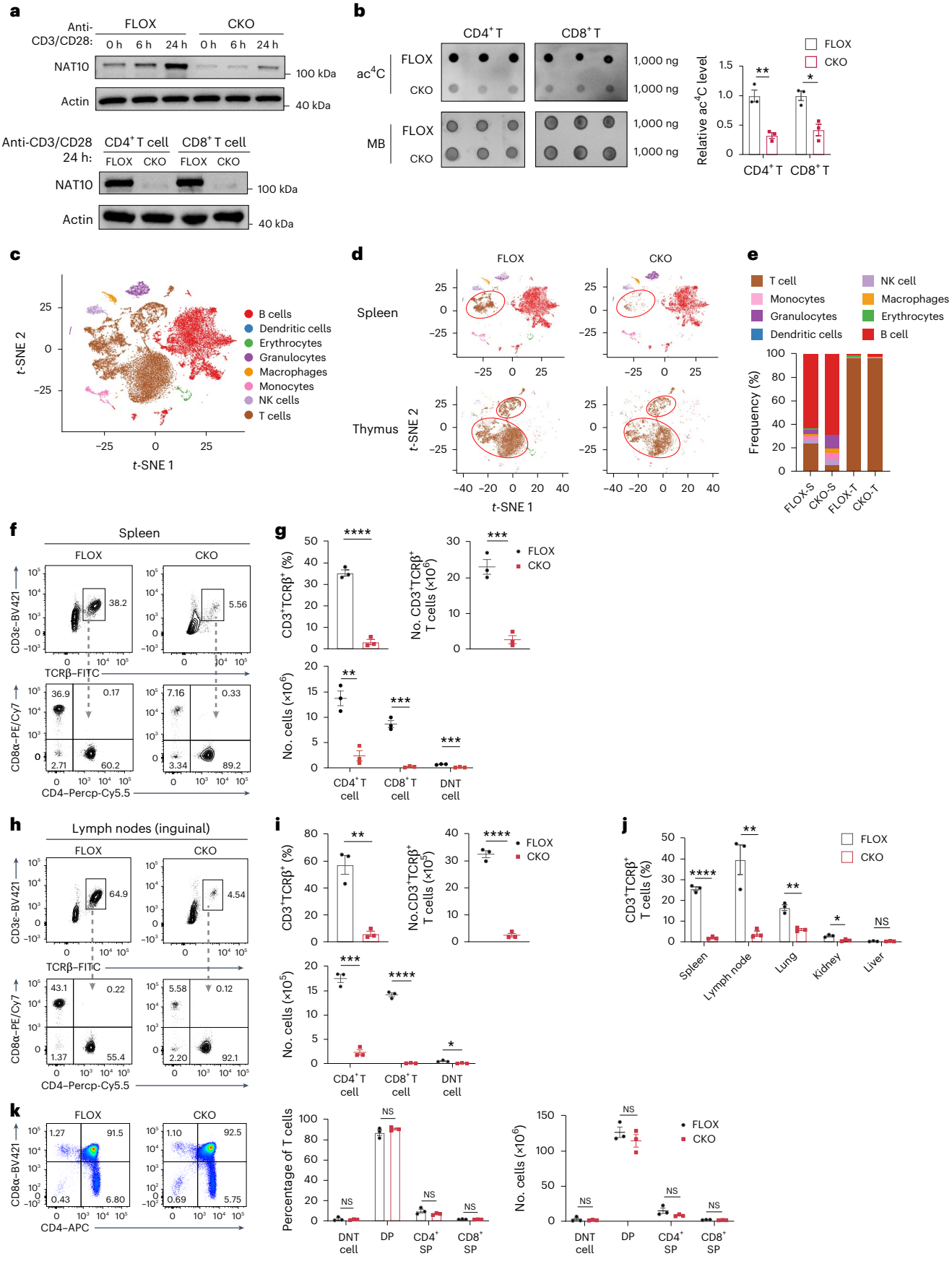

Fig. 2 | NAT10 helps to maintain the pool of T cells. a, NAT10 protein expression in $CD3^+$ T_N cells stimulated with anti-CD3/CD28 for the indicated lengths of time (top) or $CD4^+$ and $CD8^+$ T_N cells stimulated for 24 h from FLOX and CKO mice (bottom). **b**, Dot blot and densitometry analysis of ac^4C modifications in total RNA (1,000 ng) from $CD4^+$ and $CD8^+$ T_N cells stimulated with anti-CD3/CD28 for 24 h. Left, representative anti-ac^4C dot blot. Right, bar graph showing the relative ac^4C intensities quantified by methylene blue; $n = 3$; $^{**}P = 0.0037$ and $^{*}P = 0.0103$. **c**, Comprehensive *t*-SNE visualization of splenic and thymic single cells from 6- to 8-week-old FLOX and CKO mice by cell type; NK, natural killer. **d**, Separate displays of **c** by different group, with the same color coding. **e**, Bar plot showing the percentages of each cluster across groups; related to **d**; S, splenic; T, thymic. **f**, Representative FCM plots of splenic $CD3^+TCR\beta^+$, $CD4^+$ and $CD8^+$ T cells in 8-week-old FLOX and CKO mice in vivo. **g**, Percentage of $CD3^+TCR\beta^+$ T cells and absolute numbers of $CD3^+TCR\beta^+$, $CD4^+$, $CD8^+$ and double-negative (DN) T cells in the spleens of FLOX and CKO mice; $n = 3$; $^{****}P < 0.0001$, $^{***}P_{\text{No. CD3+ TCR}\beta+} = 0.0010$, $^{***}P_{\text{No.CD8+}} = 0.0003$, $^{***}P_{\text{No. DN}} = 0.0008$ and $^{**}P = 0.0031$. **h**, Representative FCM plots of $CD3^+TCR\beta^+$, $CD4^+$ and $CD8^+$ T cells in inguinal lymph nodes of FLOX and CKO mice. **i**, Percentage of $CD3^+TCR\beta^+$ T cells and absolute number of $CD3^+TCR\beta^+$, $CD4^+$, $CD8^+$ and double-negative T cells in inguinal lymph nodes of FLOX and CKO mice; $n = 3$; $^{****}P < 0.0001$, $^{***}P = 0.0001$, $^{**}P = 0.0022$ and $^{*}P = 0.0183$. **j**, Proportions of $CD3^+TCR\beta^+$ T cells in spleen, lymph node, lung, kidney and liver of FLOX and CKO mice; $n = 3$. $^{****}P < 0.0001$, $^{**}P_{\text{Lymph node}} = 0.0081$, $^{**}P_{\text{Lung}} = 0.0022$ and $^{*}P = 0.0104$; NS (not significant), $P > 0.05$. **k**, Thymic double-negative, double-positive (DP) and $CD4^+$ and $CD8^+$ single-positive (SP) T cells in FLOX and CKO mice. Left, representative FCM plots. Right, bar graphs showing proportions and absolute numbers of indicated thymic populations in FLOX and CKO mice; $n = 3$. *n* refers to the number of biologically independent samples. Error bars represent mean ± s.e.m. (**b**, **g** and **i**–**k**). Representative data of three independent experiments are presented (**a**). Data were analyzed by two-tailed, unpaired *t*-test (**b**, **g** and **i**–**k**).

Loss of NAT10 causes impaired T cell proliferation and enhanced apoptosis

To determine why CKO T cells significantly decreased in number, we performed a series of proliferation experiments. First, T_N cells from $CD45.1^+$ FLOX and $CD45.2^+$ CKO mice were isolated for in vivo proliferation assays. Cells from the two groups were labeled using CellTrace, mixed at a 1:1 ratio and transferred into *Rag2*$^{-/-}$ mice. Ninety-six hours later, proportion and CellTrace dilution analyses were performed via FCM (Fig. 3a). We observed that recipients contained significantly lower percentages of donor T cells from CKO mice than from FLOX controls (Fig. 3b). Consistently, T cells presented a remarkable proliferative defect following *Nat10* deletion (Fig. 3b). T_N cells from CKO mice that were labeled with carboxyfluorescein diacetate succinimidyl ester (CFSE) in vitro also showed impaired expansion potential (Fig. 3c). Furthermore, CKO T cells failed to increase in size, as determined by the smaller granularity detected via FCM, suggesting NAT10's critical role in regulating cell growth (Fig. 3c). We next performed cell cycle analysis to determine which stage the CKO T cells were arrested in. BrdU/7-AAD double staining showed that the fraction of cells that entered into S phase significantly decreased, with more arrested in the G0–G1 phase in CKO T cells (Fig. 3d). Another factor influencing T cell population size was the rate of apoptosis. We found that both early and late apoptosis of splenic T cells was increased in CKO mice compared to in FLOX mice, as was also the case in T cells from the lymph node (Fig. 3e,f). Together, these abnormalities in proliferation and apoptosis contribute to dramatic shrinkage of the CKO T cell pool.

NAT10 is required for the stability and translation of *Myc* mRNA

To investigate the specific mechanism of the observation above, we conducted RNA-seq using RNAs isolated from sorted splenic $CD3^+$ T_{EFF} cells. In total, 1,822 upregulated and 1,586 downregulated mRNAs were identified, with many cell division-related genes, such as *Cdk2*, *Cdk4* and *Cdc25a*, expressed at lower levels (Fig. 4a). Genes that were decreased in expression showed a significant enrichment in gene ontology (GO) terms related to metabolic processes, indicating compromised metabolism in CKO T cells (Extended Data Fig. 3a). Acetylated RNA immunoprecipitation sequencing (acRIP–seq) was also conducted synchronously to determine NAT10's role in T cell regulation as an ac^4C writer. A total of 67,564 acetylation peaks were identified, with 4,549 downregulated and 4,209 upregulated in CKO T cells compared to in FLOX control T cells (Fig. 4b). mRNAs with significantly reduced ac^4C levels showed a high enrichment in pathways related to cell proliferation, RNA regulation and cellular anabolism (Extended Data Fig. 3b). Metagene analysis showed similar global ac^4C distributions between the two groups, with acetylated peaks enriched in the vicinity of the coding sequence in mRNAs (Fig. 4c). Bringing these two sequencing data sets together, we found that 772 transcripts showed both lower ac^4C modification levels and mRNA expression levels, and these transcripts were highly enriched in pathways mainly related to cellular metabolism, nucleocytoplasmic transport, DNA replication and so on (Fig. 4d,e). The combined analysis indicated that ac^4C-modified transcripts presented a global tendency toward decreased expression following *Nat10* deletion compared to those lacking ac^4C (Fig. 4f). Allocating to specific transcripts, we found that most of the acetylated mRNAs significantly decreased in expression in response to *Nat10* deletion, whereas modification-free transcripts showed a converse bias toward increased expression following ac^4C loss (Fig. 4g). Some feedback regulation or indirect mechanisms may play a role.

Gene set enrichment analysis (GSEA) showed that 'MYC transcriptional targets' was the most prominently downregulated gene set. The vast majority of MYC-regulated genes showed impaired expression in CKO T cells versus in FLOX T cells (Fig. 4h,i). Additionally, significantly downregulated genes were also enriched in DNA replication, cell growth and G1–S transition, suggesting defective growth and expansion processes following NAT10 loss in T cells (Extended Data Fig. 3c). We then measured MYC expression after 0, 6 and 24 h of stimulation with anti-CD3/CD28. Western blotting revealed impaired expression

Fig. 3 | Loss of NAT10 causes impaired T cell proliferation and enhanced apoptosis. a, Schematic showing the in vivo competitive proliferation assays. T_N cells isolated from 8-week-old $CD45.1^+$ FLOX and $CD45.2^+$ CKO mice were labeled with CellTrace, mixed at a 1:1 ratio and transferred into 8-week-old *Rag2*$^{-/-}$ mice. After 96 h, CellTrace dilution analysis was performed; i.v., intravenous. **b**, Proportions and CellTrace fluorescence of $CD45.1^+$ FLOX and $CD45.2^+$ CKO T cells before and 96 h after transfer. Left, representative flow plots. Top right, bar graphs showing the percentages of FLOX and CKO T cells. Bottom right, bar graphs showing the percentages of FLOX and CKO T cells divided more than once; $n = 4$; $^{****}P < 0.0001$. **c**, Left, representative plots of CFSE staining and side scatters (SSC) of 72-h, anti-CD3/CD28-stimulated FLOX and CKO T cells. Right, bar graphs showing the percentages of $CFSE^{lo}$ FLOX and CKO T cells after 72 h of stimulation; $n = 3$; $^{****}P < 0.0001$. **d**, Cell cycle analysis by BrdU/7-AAD staining of 48-h, anti-CD3/CD28-stimulated $CD4^+$ and $CD8^+$ T cells. Top, representative flow plots. Bottom, bar graphs showing the distribution of FLOX and CKO T cells across G0–G1, S and G2–M phases, respectively. $n = 4$; $^{****}P < 0.0001$. **e**, Apoptosis assessment by Annexin V/propidium iodide (PI) staining of FLOX and CKO T cells in the spleen. Top, representative flow plots. Bottom, bar graphs showing the proportions of live (Annexin V^-PI^-), early apoptotic (Annexin V^+PI^-) and late apoptotic (Annexin V^+PI^+) splenic T cells in FLOX and CKO mice; $n = 4$. Exact *P* values from left to right: $^{**}P = 0.0041$, $^{**}P = 0.0040$, $^{*}P = 0.0197$, $^{***}P = 0.0004$, $^{***}P = 0.0006$ and $^{***}P = 0.0009$. **f**, Apoptosis detection performed the same as in **e** in the lymph nodes. Left, representative flow plots. Right, bar charts showing the proportions of the indicated populations in FLOX and CKO mice (FLOX $n = 3$, CKO $n = 4$). Exact *P* values from left to right: $^{**}P = 0.0031$, $^{*}P = 0.0137$, $^{**}P = 0.0021$, $^{**}P = 0.0050$, $^{*}P = 0.0293$ and $^{**}P = 0.0053$. *n* refers to the number of biologically independent samples. Error bars represent mean ± s.e.m. (**b**–**f**). Data were analyzed by two-tailed, unpaired *t*-test (**b**–**f**).

https://doi.org/10.1038/s41590-025-02100-2

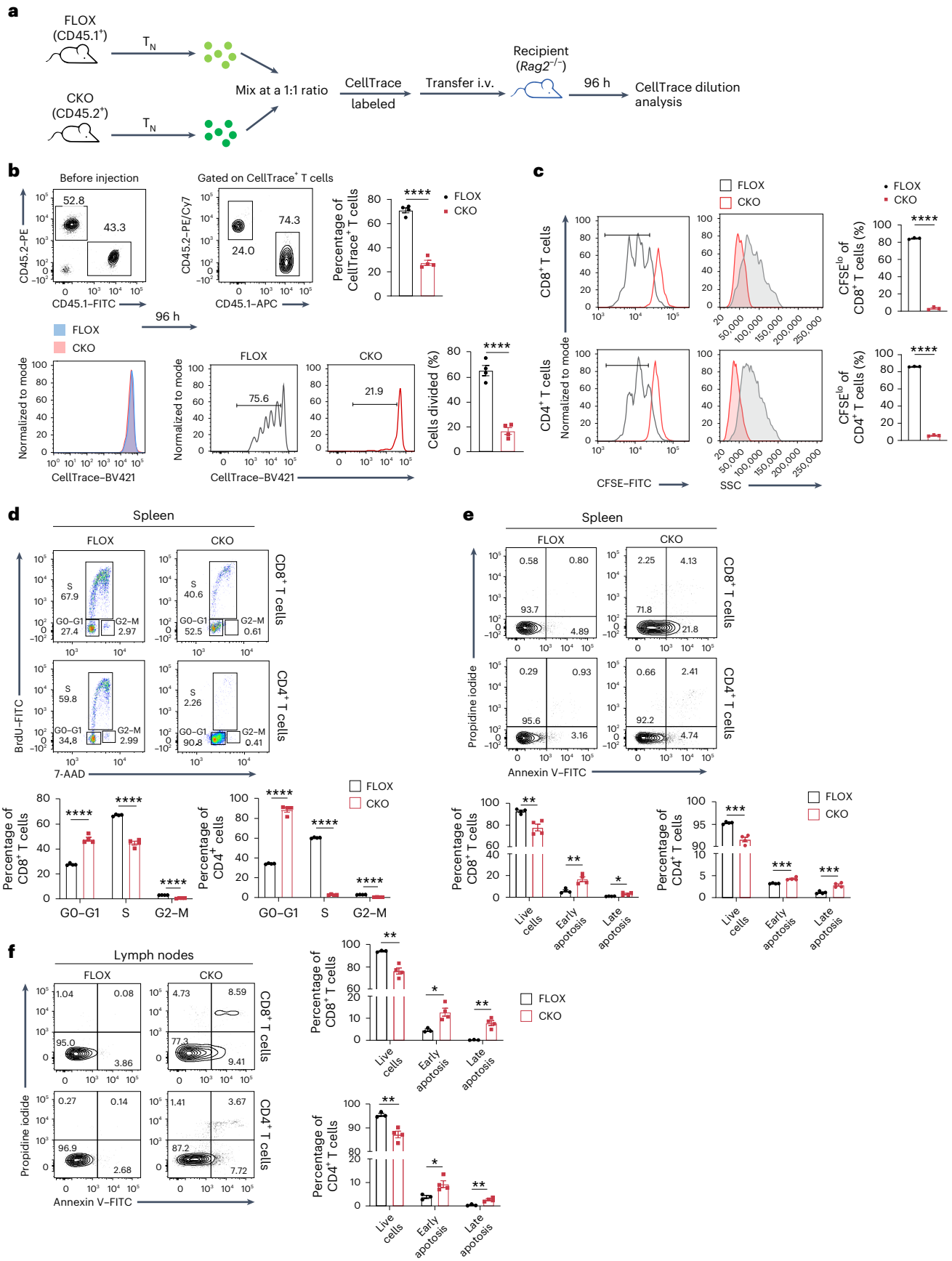

https://doi.org/10.1038/s41590-025-02100-2

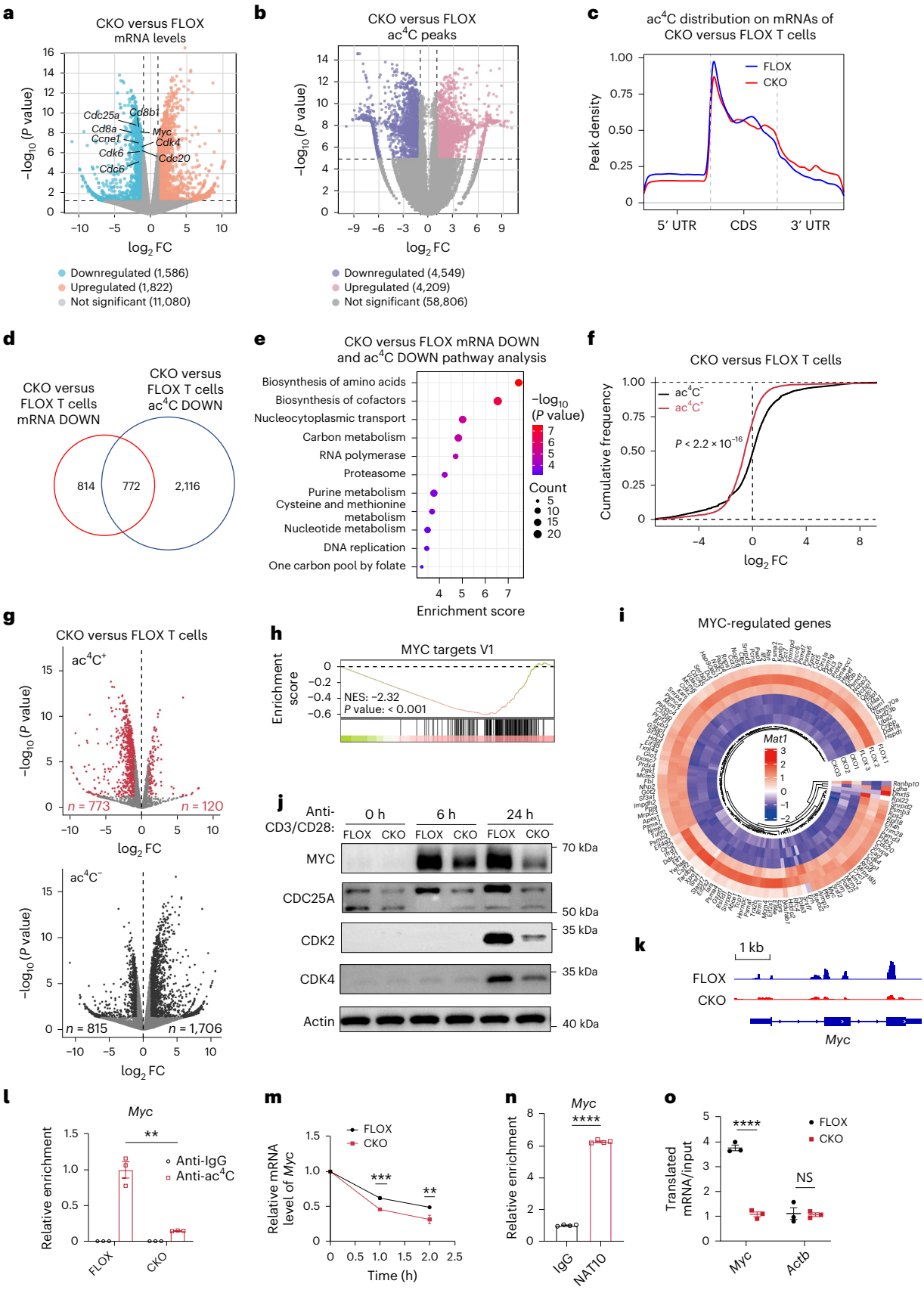

Fig. 4 | NAT10 is required for the stability and translation efficiency of *Myc* mRNA. a, Volcano plot showing differentially expressed genes between CKO and FLOX activated T_{EFF} cells, with cutoffs of $P \leq 0.05$ and | fold change | ≥ 2; FC, fold change. **b**, Volcano plot showing differentially acetylated peaks between CKO and FLOX T_{EFF} cells, with cutoffs of $P \leq 0.00001$ and | fold change | ≥ 2. **c**, Metagene analysis of ac^4C sites identified on mRNAs from FLOX and CKO T_{EFF} cells; UTR, untranslated region; CDS, coding sequence. **d**, Venn diagram showing the numbers of transcriptionally repressed transcripts with significantly fewer modified by ac^4C. **e**, KEGG pathway analysis of the overlapped genes identified in **d**. **f**, Cumulative distribution function plot exhibiting differential expression of ac^4C^+ or ac^4C^- transcripts between CKO and FLOX T_{EFF} cells. **g**, Volcano plots of differentially expressed mRNAs between CKO and FLOX T_{EFF} cells segregated by ac^4C modification, with cutoffs of $P \leq 0.05$ and | fold change | ≥ 2. **h**, GSEA of 'MYC targets V1' between CKO and FLOX T_{EFF} cells; NES, normalized enrichment score. **i**, Circular heat map showing mRNA levels of MYC-regulated genes in FLOX and CKO T_{EFF} cells. **j**, MYC, CDC25A, CDK2 and CDK4 protein levels in FLOX and CKO $CD3^+$ T_N cells stimulated with anti-CD3/CD28 for the indicated lengths of time. Representative bands of three independent experiments are presented. **k**, IGV plot displaying specific ac^4C peaks on *Myc* transcripts. Peaks are represented as subtracted read densities (IP minus input). **l**, ac^4C RIP–qPCR for *Myc* mRNA in activated FLOX and CKO $CD3^+$T cells; $n = 3$; $^{**}P = 0.0017$. **m**, Degradation of *Myc* mRNA in activated FLOX and CKO $CD3^+$ T cells 1 and 2 h after actinomycin D treatment; $n = 3$; $^{***}P = 0.0003$ and $^{**}P = 0.0097$. **n**, NAT10 RIP–qPCR for *Myc* mRNA in activated CKO and FLOX $CD3^+$ T cells; $n = 4$; $^{****}P < 0.0001$. **o**, Ribosome occupancy of *Myc* and control mRNAs in activated CKO and FLOX $CD3^+$ T cells; $n = 3$; $^{****}P < 0.0001$. *n* refers to biologically independent samples. Activated T cells were stimulated with anti-CD3/CD28 for 24 h in **l**–**o**. Error bars represent mean ± s.e.m. (**l**–**o**). Data were analyzed by two-tailed, negative binomial distribution test (**a**, **b** and **g**); one-sided, hypergeometric test (Benjamini–Hochberg adjusted) (**e**); two-tailed, Mann–Whitney *U*-test (**f**); two-tailed Kolmogorov–Smirnov test (**h**) and two-tailed, unpaired *t*-test (**l**–**o**).

of MYC at the protein level, in addition to the acknowledged MYC targets CDK2, CDK4 and CDC25A (Fig. 4j). How, then, does NAT10 impact MYC protein levels? acRIP–seq visualized by Integrated Genomics Viewer (IGV) showed that ac^4C peaks were extensively distributed within the *Myc* mRNA region, and these peaks were all significantly downregulated after *Nat10* deletion (Fig. 4k). ac^4C-RIP–qPCR further confirmed that *Myc* mRNA was ac^4C modified, and relative enrichment of ac^4C peaks was reduced by about 85% in CKO T cells compared to in FLOX control T cells (Fig. 4l). To verify whether this was because of decreased ac^4C abundance and subsequent impaired stability of modified transcripts, we adopted an in vitro assay using actinomycin D (a transcription inhibitor) to investigate the speed of *Myc* RNA decay. We observed that the degradation velocity for *Myc* was faster for CKO T cells than for FLOX control T cells (Fig. 4m). Except for ac^4C, NAT10 protein was also shown to bind to *Myc* mRNA specifically (Fig. 4n). To further explore the influence of ac^4C on mRNA translation within T cells, we performed ribosome profiling (Ribo-seq). Briefly, ribosome-protected fragments (RPFs) were collected, sequenced and projected to the total transcripts shown in the RNA sequence, contributing to measuring ribosome density, namely translation efficiency (TE). T cell transcripts were classified into two categories, ac^4C^+ and ac^4C^-, according to the presence or absence of ac^4C peaks revealed by ac^4C RIP–seq. The sequencing data showed that ac^4C^+ transcripts manifested markedly higher TE than ac^4C^- transcripts, guaranteeing efficient protein synthesis in $CD3^+$ T cells (Extended Data Fig. 3d). Furthermore, compared to FLOX control T cells, TE of ac^4C^- mRNAs stayed unchanged, whereas that of ac^4C^+ transcripts showed a significant decrease in CKO T cells, indicating that *Nat10* KO ablated the elevation of TE due to ac^4C modification in T cells (Extended Data Fig. 3d). Focusing on *Myc* mRNA, we performed polyribosome real-time PCR and found a dramatic decrease in the accumulation of ribosomes on *Myc* but not on control transcripts in CKO T cells (Fig. 4o). In summary, NAT10 promotes the synthesis of MYC protein by facilitating mRNA stability and translation.

Nat10 deletion causes metabolic dysfunction of T cells

Except for direct MYC transcriptional targets, the related metabolic gene sets were also significantly compromised at the transcription level (Extended Data Fig. 4a). According to 'Compass' analysis, an algorithm that evaluates the metabolic state of cells based on scRNA-seq data, cellular metabolism was broadly impaired in CKO T cells[17]. Metabolic reactions, including nucleotide, lipid, carbohydrate, amino acid and energy metabolism and so on, showed significantly decreased activity in response to NAT10 loss (Extended Data Fig. 4b). Adequate supplies and instant reprogramming in metabolism are both critical for T cell activation and expansion. We next performed ultraperformance liquid chromatography–tandem mass spectrometry (UPLC–MS/MS) analysis of FLOX and CKO T_N cells as well as their activated counterparts to see if NAT10 deficiency impaired this intricate metabolic network. We observed that levels of most nucleotides, amino acids and fatty acids were robustly elevated in stimulated FLOX T cells. However, this metabolic reprogramming was compromised after *Nat10* deletion (Extended Data Fig. 4c,d and Supplementary Tables 1 and 2). Additionally, decreased glucose uptake and extracellular acidification rate (ECAR) suggested lower levels of glycolysis during activation in CKO T cells (Extended Data Fig. 4e,f). Reduced oxygen consumption rate (OCR) and ATP production in both CKO T_N and T_{EFF} cells suggest dysfunctional energy supplies in T cells without NAT10 support (Extended Data Fig. 4f,g). That is, metabolic dysfunction due to NAT10 deficiency fails to fuel the robust biosynthesis required for activation-induced cell growth and proliferation in CKO T cells.

NAT10 overexpression rescues proliferative defects in CKO T cells

To verify the contribution of the NAT10–MYC axis to the phenotypes of CKO T cells, we constructed bone marrow chimeric mice with hematopoietic stem cells (HSCs) from FLOX and CKO mice, respectively. NAT10 or MYC was overexpressed in CKO HSCs via retroviruses, and

Fig. 5 | NAT10 overexpression rescues proliferative defects in CKO T cells. a, Schematic diagram showing construction of bone marrow chimeric mice. $CD117^+$ enriched HSCs from 8-week-old FLOX and CKO mice were infected with control or NAT10- or MYC-overexpressing retrovirus and then transplanted into irradiated 8-week-old $CD45.1^+$ mice. Ten weeks later, $CD45.2^+$ T cells derived from retrovirus-infected HSCs were identified for further proliferation analysis. **b**, NAT10 and MYC overexpression in CKO T cells was verified by immunoblotting. Representative bands of three independent experiments are presented; NC, negative controls. **c**, Frequency of $CD4^+$ and $CD8^+$ T cells as a proportion of total adoptive cells identified by CD45.2 staining in each group. Left, representative flow plots. Right, bar graphs showing the percentage of $CD4^+$ and $CD8^+$ T cells from total adoptive cells; $n = 3$. For data from the spleen, $^{***}P_{CD8+} = 0.0002$, $^{**}P_{CD8+} = 0.0015$, $^{*}P_{CD8+} = 0.0488$, $^{**}P_{CD4+} = 0.0037$ and $^{*}P_{CD4+} = 0.0174$. For data from the lymph nodes, $^{****}P < 0.0001$, $^{***}P = 0.0005$ and $^{**}P = 0.0041$. **d**,**e**, CellTrace dilution analysis of T cells from chimeric mice. T cells labeled by CellTrace were activated with anti-CD3/CD28 for 72 h and detected via FCM. Representative flow plots are shown on the top (**d**) or left (**e**), and bar plots displaying percentages of $CellTrace^{lo}$ activated T cells in each group are shown on the bottom (**d**) or right (**e**); $n = 4$; $^{****}P < 0.0001$. **f**, O-propargyl-puromycin (OPP) staining of activated T cells (stimulated with anti-CD3/CD28 for 24 h) from chimeric mice. Left, representative flow plots. Right, bar plots displaying the percentages of OPP^+ T cells in each group; $n = 3$; $^{****}P < 0.0001$. *n* refers to the number of biologically independent samples. Error bars represent mean ± s.e.m. (**c**–**f**). Data were analyzed by two-tailed, one-way ANOVA with Tukey's multiple comparisons test (**c**–**f**).

https://doi.org/10.1038/s41590-025-02100-2

negative control plasmids were also transfected into HSCs from both groups as baseline controls. Treated HSCs accompanied with moderate protectors were then transferred into irradiated CD45.1$^+$ mice (Fig. 5a). Ten weeks later, CD45.2$^+$ T cells derived from retrovirus-infected HSCs were identified for further analysis. Overexpression in T cells was validated by western blotting (Fig. 5b). NAT10 overexpression efficiently reverted the T cell pool (Fig. 5c). More importantly, the proliferative defect following TCR stimulation in CKO T cells was effectively compensated by NAT10 or MYC restoration (Fig. 5d,e). The same was true for protein synthesis potency (Fig. 5f). Together, these data

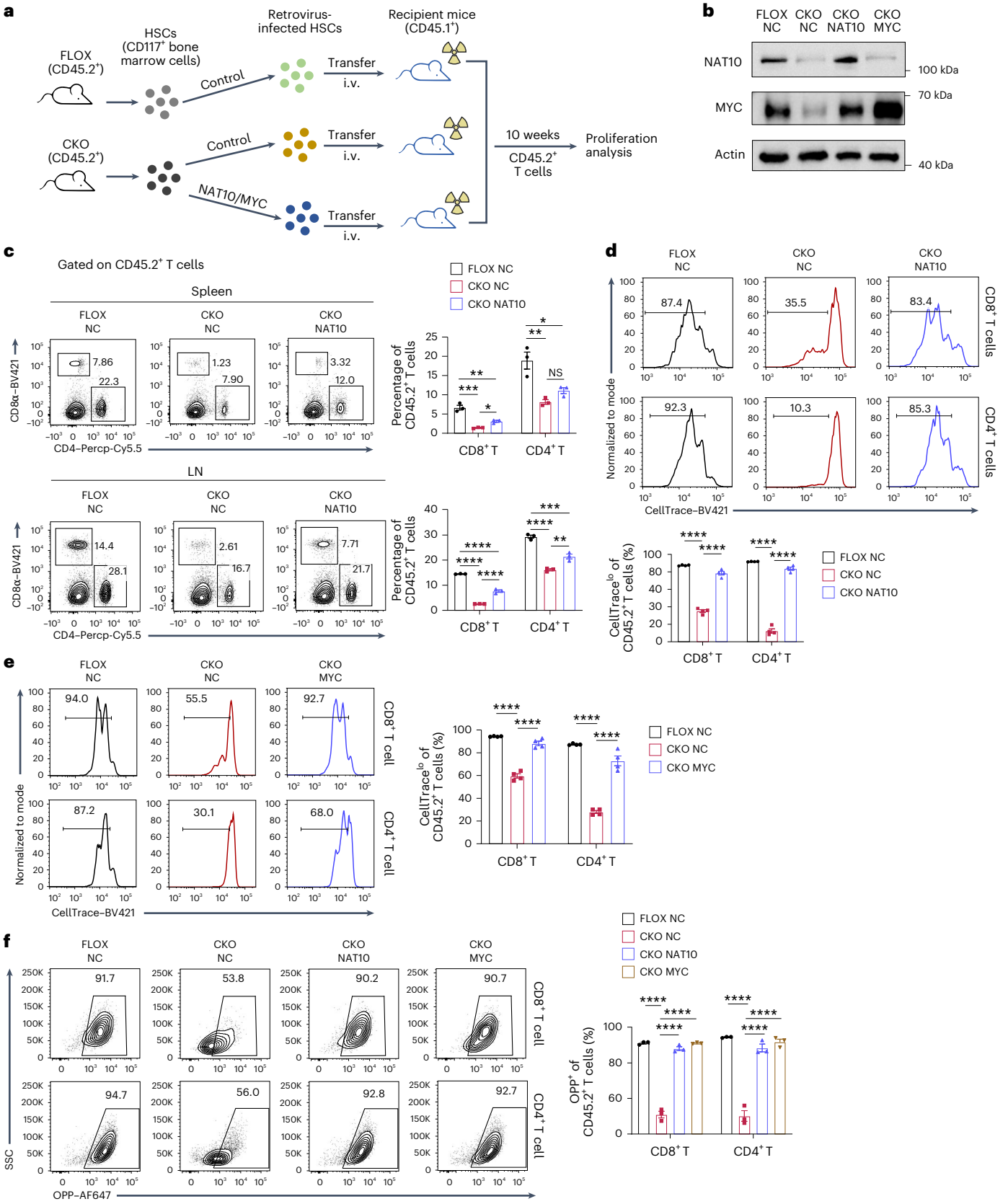

demonstrate that the proliferative and metabolic defects in CKO mice were largely dependent on the NAT10–MYC axis, suggesting its critical role in T cell maintenance and expansion.

NAT10 matters in T cell antiviral immunity

T cells have long been considered a vital player in antiviral response. The robust expansion capacity serves as an important prerequisite for activated T cells to be excellent virus defenders. Considering NAT10's core role in T cell proliferation, we next sought to determine whether NAT10 is involved in T cell antiviral potency.

Age- and sex-matched FLOX and CKO mice were infected with LCMV Armstrong as previously described to develop an acute LCMV infection model, with mice injected with PBS serving as controls. Animals were killed at 8, 16 and 24 days after infection (Fig. 6a). Virus load analysis revealed that CKO mice harbored 11-fold higher viral RNA in the serum than FLOX control mice on day 8 after infection, indicating severe antiviral defects of T cells following NAT10 deficiency (Fig. 6b). Additionally, we found that spleens and lymph nodes in FLOX mice were greatly enlarged, suggesting robust proliferation of lymphocytes during virus infection, which was significantly attenuated in CKO mice (Fig. 6c). Consistently, the absolute numbers of splenic $CD8^+$ and $CD4^+$ T cells from CKO mice were also remarkably less (Fig. 6d). To further evaluate the role of NAT10 in T cell responses during virus infection, tetramer staining and FCM were performed on spleen, lymph node and peripheral blood from infected mice. Results showed that the proportion of LCMV-specific $CD8^+$ T cells in the above tissues from CKO mice was significantly lower than that from FLOX control mice (Fig. 6e,f). The absolute number of splenic $GP33^+CD8^+$ T cells and functional $CD8^+$ T cells secreting IFNγ and TNF presented a similar variation (Fig. 6g,h). In addition, key cytokines related to virus killing (IFNγ and TNF) and IL-2 in the serum were found at lower levels in CKO mice at 4 and 8 days after infection, respectively (Fig. 6i). At days 16 and 24 after LCMV infection, the proportion of virus-specific T cells in CKO mice was still at a diminished level (Fig. 6j). Twenty-four days after infection, the proportion of the $KLRG1^{lo}CD127^{hi}$ subset in $GP33^+$ T cells was also significantly decreased in CKO mice, suggesting impaired memory T cell formation following NAT10 deficiency (Fig. 6k).

$CD8^+$ T cells from P14 mice (with transgenic expression of H-2Db-restricted TCR specific for LCMV glycoprotein 33–41) can recognize the LCMV $GP_{33–41}$ peptide and produce robust LCMV-specific $CD8^+$ T cell responses. We then generated P14 T cells with *Nat10* knockdown via retroviruses and transferred the cells to naive WT mice 1 day before LCMV Armstrong infection (Extended Data Fig. 5a,b). Three days later, transfected T cells were identified, and remarkable proliferative impairment was observed in *Nat10*-knockdown P14 T cells (Extended Data Fig. 5c). Seven days after infection, the percentage, absolute number and amplification fold change of P14 T cells were all found to be significantly decreased following NAT10 deficiency (Extended Data Fig. 5d). Functional defenders ($TNF^+IFNγ^+$ P14 T cells) exhibited the same trend (Extended Data Fig. 5e).

Together, NAT10 matters in T cell antiviral immunity. Loss of NAT10 causes contraction of the T cell population along with compromised in vivo antiviral responses in mice.

Decreased NAT10 levels in T cells from older individuals may be involved in age-related antiviral defects

Interestingly, we found an age-related differential NAT10 expression in both human immune cells and mouse immune organs. In mice, NAT10 protein levels were significantly diminished in the spleens of 72-week-old mice compared to in 8-week-old young control mice (Fig. 7a). This decrease was also confirmed at the ac^4C level (Fig. 7b). We then performed RNA-seq and acRIP–seq in spleens from young (aged 8 weeks) and old (aged 72 weeks) mice to determine changes in ac^4C modifications in immune organs during aging and NAT10's potential role in it (Extended Data Fig. 6a). GO analysis of significantly downregulated genes in old spleens versus in the spleens of young control mice from RNA-seq data sets showed dampened adaptive immune responses and reduced T cell activation in aged mice (Extended Data Fig. 6b). According to the epitranscriptome profiling, the global distribution patterns of ac^4C in the spleen as reported were similar between young and old mice (Extended Data Fig. 6c). Additionally, CUWCV and UWYMU were identified ac^4C sequence motifs in the spleens of young and old mice, respectively (Extended Data Fig. 6d). To further determine expression changes in response to ac^4C loss, we performed combined mRNA-seq and acRIP–seq analyses. Among 630 transcripts with decreased ac^4C modifications, 65 were also lower at the mRNA level (Supplementary Table 3). These potential NAT10 targets showed high enrichment in GO analysis terms related to T cells, such as T cell activation, differentiation and proliferation (Extended Data Fig. 6e). These data link NAT10 to age-associated T cell alterations.

Next, to determine NAT10 expression in T cells at different ages more specifically, we purified $CD3^+$ splenic T cells from young (8-week-old) and old (72-week-old) mice and stimulated them with anti-CD3/CD28 for the indicated lengths of time. Western blot analysis suggested that NAT10 was downregulated in T cells from old mice (Fig. 7c). Changes in MYC protein expression showed a similar trend, as did MYC expression in CKO T cells (Fig. 7c). Additionally, an identical proliferation defect was also observed in T cells from aged mice (Fig. 7d).

In humans, peripheral blood mononuclear cells (PBMCs) from older (≥60 years old) and younger (<60 years old) healthy donors were purified by Ficoll gradient centrifugation and stimulated by treatment with anti-CD3/CD28 in the presence of IL-2 for 48 h (Extended Data Fig. 6f). These populations, over 75% of which were T cells, were then analyzed by western blotting (Extended Data Fig. 6g). Results showed that NAT10 protein expression was attenuated in activated T cells from older individuals compared to in activated T cells from young control individuals, with MYC showing a similar trend (Fig. 7e). Expansion of T cells obtained from older individuals was also impaired (Fig. 7f).

Fig. 6 | NAT10 matters in T cell antiviral immunity. a, Schematic of the acute LCMV infection model in FLOX and CKO mice. Eight-week-old FLOX and CKO mice were intraperitoneally injected with 2×10^5 p.f.u. LCMV Armstrong and killed at 8, 16 and 24 days after infection. Animals treated with equal volumes of PBS served as blank controls. Serum, spleens and lymph nodes from the LCMV group were collected for further analysis. **b**, Viral loads in the serum derived from FLOX ($n = 9$) and CKO ($n = 10$) mice at 8 days after LCMV administration; $^*P = 0.0253$. **c**, Gross appearance of spleens and inguinal lymph nodes from infected FLOX and CKO mice and their blank controls at 8 days after PBS or virus administration. **d**, Absolute number of splenic $CD8^+$ and $CD4^+$ T cells in FLOX ($n = 8$) and CKO ($n = 10$) infected mice at 8 days after infection; $^{****}P < 0.0001$. **e**,**f**, Percentages of $GP33^+CD44^+$ $CD8^+$ T cells in the spleen, lymph node and blood from FLOX ($n = 6$, 6 and 6) and CKO ($n = 4$, 4 and 3) infected mice at 8 days after infection; $^{****}P < 0.0001$ and $^{***}P = 0001$. **g**, Absolute number of splenic $GP33^+CD44^+$ $CD8^+$ T cells from FLOX ($n = 6$) and CKO ($n = 4$) infected mice at 8 days after infection; $^{****}P < 0.0001$. **h**, Absolute number of splenic $IFNγ^+$ and $IFNγ^+TNF^+$ $CD8^+$ T cells in FLOX ($n = 8$) and CKO ($n = 9$) infected mice at 8 days after infection; $^{****}P < 0.0001$ and $^{***}P = 0.0006$. **i**, Serum IL-2, IFNγ and TNF (8, 4 and 4 days after infection, respectively) levels in FLOX and CKO infected mice ($n = 6$); $^{****}P < 0.0001$, $^{***}P = 0.0007$ and $^*P = 0.0141$. **j**, Percentages of $GP33^+CD44^+$ $CD8^+$ T cells in blood from FLOX ($n = 5$, 6 and 6) and CKO ($n = 3$, 5 and 5) infected mice at 8, 16 and 24 days after infection; $^{****}P < 0.0001$. **k**, Percentages of $GP33^+$ $CD8^+$ T cells (FLOX $n = 6$, CKO $n = 5$) and $KLRG1^{lo}CD127^{hi}GP33^+$ $CD8^+$ T cells (FLOX $n = 6$, CKO $n = 3$) from FLOX and CKO infected mice at 24 days after infection; $^{****}P < 0.0001$ and $^{***}P = 0.0003$. *n* refers to the number of biologically independent samples. Error bars represent mean ± s.e.m. (**b**, **d** and **f**–**k**). Data were analyzed by two-tailed, unpaired *t*-test (**b**, **d**, **f**–**i** and **k**) or two-tailed, two-way ANOVA with Šídák's multiple comparisons test (**j**).

https://doi.org/10.1038/s41590-025-02100-2

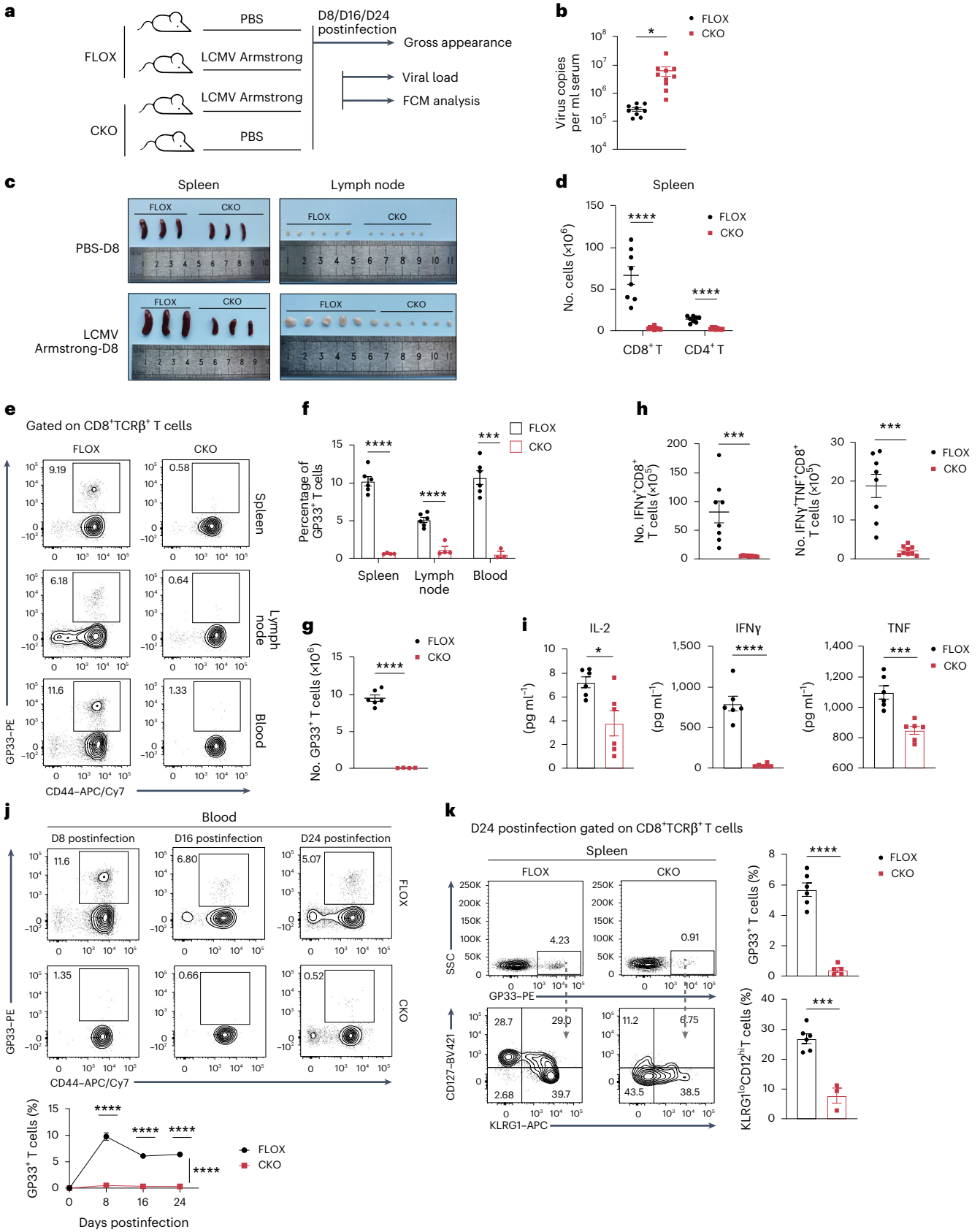

It is well known that older individuals are usually more susceptible to viral infection than those that are younger, with longer duration and more severe symptoms, which is largely related to aging of the immune system[18]. To further inspect if NAT10 plays a parallel role in human antiviral responses, as it does in our mouse model, we reanalyzed published RNA-seq data from leukocytes derived from individuals with coronavirus disease 2019 (COVID-19)[19]. A total of 98 individuals were included, with 3 excluded for missing age data and 1 excluded as an outlier (with NAT10 and MYC expression values outside the mean ± 2.5 s.d.). In this cohort, individuals with mild or moderate symptoms were admitted to the hospital with only supportive care, whereas those with critical symptoms were admitted to the intensive care unit (ICU). Therefore, we placed individuals not in the ICU in the 'none-severe' group ($n = 49$) and placed individuals in the ICU in the 'severe' group ($n = 49$), as in other studies[20]. Fifty-six of the 98 individuals were older (>60 years old), and the others belonged to the young group (≤60 years old; $n = 42$). Results showed that individuals with serious COVID-19 symptoms expressed lower levels of *NAT10* and *MYC* in both young and old groups (Fig. 7g). Additionally, consistent with our in vitro data, *NAT10* and *MYC* were also expressed at lower levels in older individuals than in younger individuals in both none-severe and severe groups (Fig. 7h). Pearson's correlation analysis suggested that NAT10 protein levels were significantly positively correlated with MYC expression (Fig. 7i). The APACHEII score is widely used to assess disease severity and prognosis, with a higher score indicating a more critical condition. Among the participants, we observed a significant inverse correlation between NAT10 expression and severity of clinical symptoms (Fig. 7j). The same was true for MYC (Fig. 7j). Thus, NAT10 expression in leukocytes is negatively associated with age and severity. However, it remains unknown how it works. Numerous factors may be involved in this process. For example, it is recognized that individuals with severe COVID-19 show marked decreases in lymphocyte populations[21]. Decreased NAT10 abundance may contribute to this lymphopenia, and alterations in lymphocytes may also in turn impact NAT10 levels in individuals with severe disease. These intricate relationships await to be further elucidated.

To further investigate the role that NAT10 plays in human antiviral responses, we reanalyzed published COVID-19 scRNA-seq data[22], with 41 personal samples included. These individuals were classified into healthy (WHO score of 0), none-severe (WHO score of 1–5) and severe (WHO score of 6–8) groups[22] and partitioned into young (<60 years old) and old (≥60 years old) groups by age. Around 110,000 thousand high-quality single cells were obtained in total, and 14 cell clusters were derived after UMAP dimension reduction analysis, covering diverse cell types in peripheral blood (Extended Data Fig. 6h). Natural killer cells and T cells were then purified for deeper analysis, with 18 clusters displayed at a higher resolution (Extended Data Fig. 6i). We next compared *NAT10* expression at the transcript level across all subpopulations. As we expected, *NAT10* was most highly expressed in proliferating T cells (Fig. 7k). In addition, we found that both in cases of none-severe and severe COVID-19, older individuals exhibited a significant reduction in $CD8^+$ proliferative T cells compared to younger individuals (Fig. 7l). Reports have indicated that there may be considerable differences in immune status among individuals with varying degrees of symptom severity. T cells can be profoundly depleted for strong antiviral responses in individuals with severe disease[23]. Acute lymphopenia serves as a strong signal to induce T cell proliferation, and perhaps that is part of what causes increasing numbers of proliferative T cells in individuals with severe disease[24,25]. Elevated numbers of proliferating populations may help to maintain the T cell pool against severe COVID-19. However, this increase of proliferating subsets induced by symptom exacerbation is significantly reduced in the older population, which may be partially responsible for their impaired antiviral responses against severe acute respiratory syndrome coronavirus 2 (SARS-CoV-2).

NAT10 overexpression restores proliferation and antiviral defects in T cells from older individuals

Given the role of the NAT10–MYC axis in age-associated antiviral decline, we next explored whether NAT10 or MYC overexpression in old T cells could reverse their impaired expansion capacity. T cells with retroviral infection were identified by green fluorescent protein (GFP) expression for further analysis. Overexpression efficiency was verified by western blotting (Fig. 8a). As expected, protein levels of MYC targets were efficiently upregulated in T cells from old mice following NAT10 restoration (Fig. 8a). CellTrace dilution analysis and Ki-67 staining indicated that NAT10 or MYC overexpression could functionally compensate for proliferative defects in aged T cells (Fig. 8b,c). Additionally, the decrease in metabolic activity was also reverted. Significant reductions in glucose consumption, lactate production, ATP generation and protein synthesis in T cells from aged mice were all recovered by NAT10 or MYC restoration to different degrees (Fig. 8d–g). Thus, NAT10 or MYC overexpression can efficiently improve both proliferative and metabolic defects in T cells from older animals.

Further, the in vivo LCMV infection model was applied to investigate if NAT10 upregulation could improve the antiviral responses of aged T cells. $CD8^+$ T cells obtained from old P14 mice with control or *Nat10*-overexpressing plasmids were transferred into *Rag2*$^{-/-}$ mice 1 day before LCMV infection (Fig. 8h). According to our results, recipients with NAT10-overexpressing P14 T cells harbored lower viral RNA levels in serum than their control counterparts on day 8 after LCMV infection (Fig. 8i). Additionally, NAT10-overexpressing P14 T cells were found to amplify at a higher rate and contained more functional defenders ($TNF^+IFN\gamma^+$ T cells; Fig. 8j,k). That is to say, NAT10 restoration efficiently

Fig. 7 | Decreased NAT10 levels in T cells from older individuals might be involved in age-related antiviral defects. a,**b**, NAT10 protein (**a**) and ac^4C (**b**) levels in splenocytes from young (8 weeks (8w)) and old (72 weeks (72w)) mice. The bar graph in **b** shows the relative ac^4C intensities normalized to total RNA (200 ng); $n = 3$; $^{**}P = 0.0034$. **c**, NAT10 and MYC expression levels in $CD3^+$ T cells from young (8 weeks) and old (72 weeks) mice stimulated with anti-CD3/CD28 for the indicated lengths of time. **d**, CellTrace dilution of 72-h, anti-CD3/CD28-stimulated T cells from young (8 weeks) and old (72 weeks) mice. Left, representative flow plots. Right, bar graphs showing percentages of $CellTrace^{lo}CD3^+$ T cells from young and old mice, respectively; $n = 3$; $^{**}P = 0.0088$. **e**, NAT10 and MYC protein levels in 48-h, anti-CD3/CD28-stimulated PBMCs from healthy young (<60 years old, three men and two women) and older (≥60 years old, three men and two women) adults. **f**, CFSE dilution of 72-h, anti-CD3/CD28-stimulated $CD3^+$ T cells from young (<60 years old) and older (≥60 years old) healthy donors. Left, representative flow plots. Right, bar graphs showing percentages of $CFSE^{lo}CD3^+$ T cells in young ($n = 5$) and older ($n = 4$) healthy donors; $^*P = 0.0218$. **g**,**h**, Box plots showing NAT10 and MYC expression between none-severe and severe groups of the same age category (**g**) or between young (<60 years old) and older (≥60 years old) groups with similar disease severity (**h**; young none-severe $n = 26$, young severe $n = 16$, old none-severe $n = 23$, old severe $n = 33$). Boxes show median and top and bottom quartiles, whiskers show 1.5× interquartile range on either side, and points show independent samples. **i**, Correlation analysis between NAT10 and MYC expression in individuals with COVID-19; $n = 98$. **j**, Correlation analysis between APACHEII scores and NAT10 and MYC expression in individuals with COVID-19; $n = 56$. **k**, NAT10 expression across clusters identified in Extended Data Fig. 6i. **l**, Proportions of $CD8^+$ proliferating T cells in young none-severe ($n = 14$), old none-severe ($n = 4$), young severe ($n = 8$) and old severe ($n = 5$) individuals, respectively. *n* refers to the number of biologically independent samples. Representative data from three independent experiments are presented (**c** and **e**). Error bars represent mean ± s.e.m. (**b**, **d** and **f**). Data were analyzed by two-tailed, unpaired *t*-test (**b**, **d**, **f**–**h** and **l**) or two-tailed, Pearson correlation method (**i** and **j**); T_{CM}, central memory T cell; MAIT, mucosal-associated invariant T cells; T_{reg}, regulatory T cells; T_{EM}, effector memory T cells; CTL, cytotoxic T lymphocytes.

https://doi.org/10.1038/s41590-025-02100-2

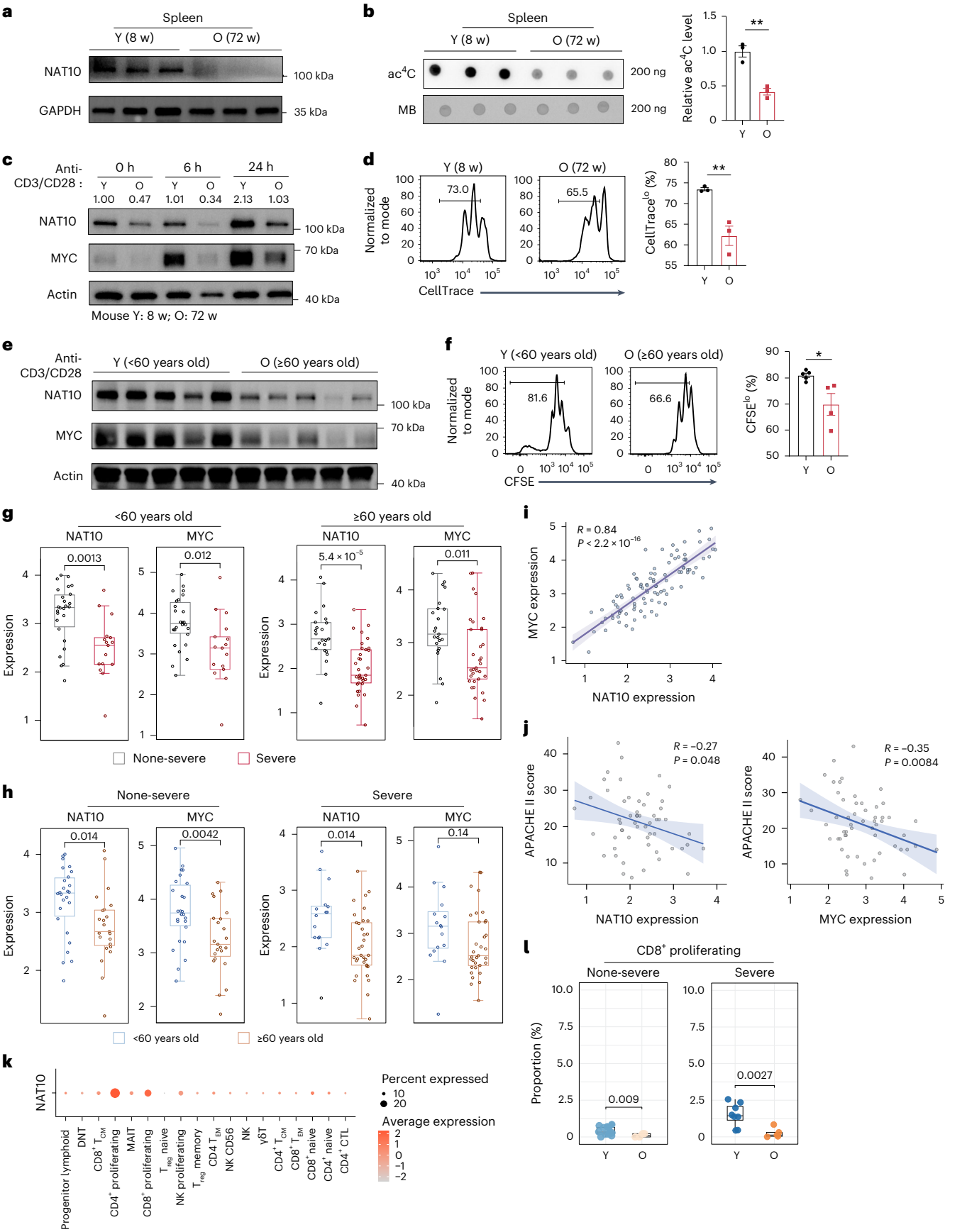

https://doi.org/10.1038/s41590-025-02100-2

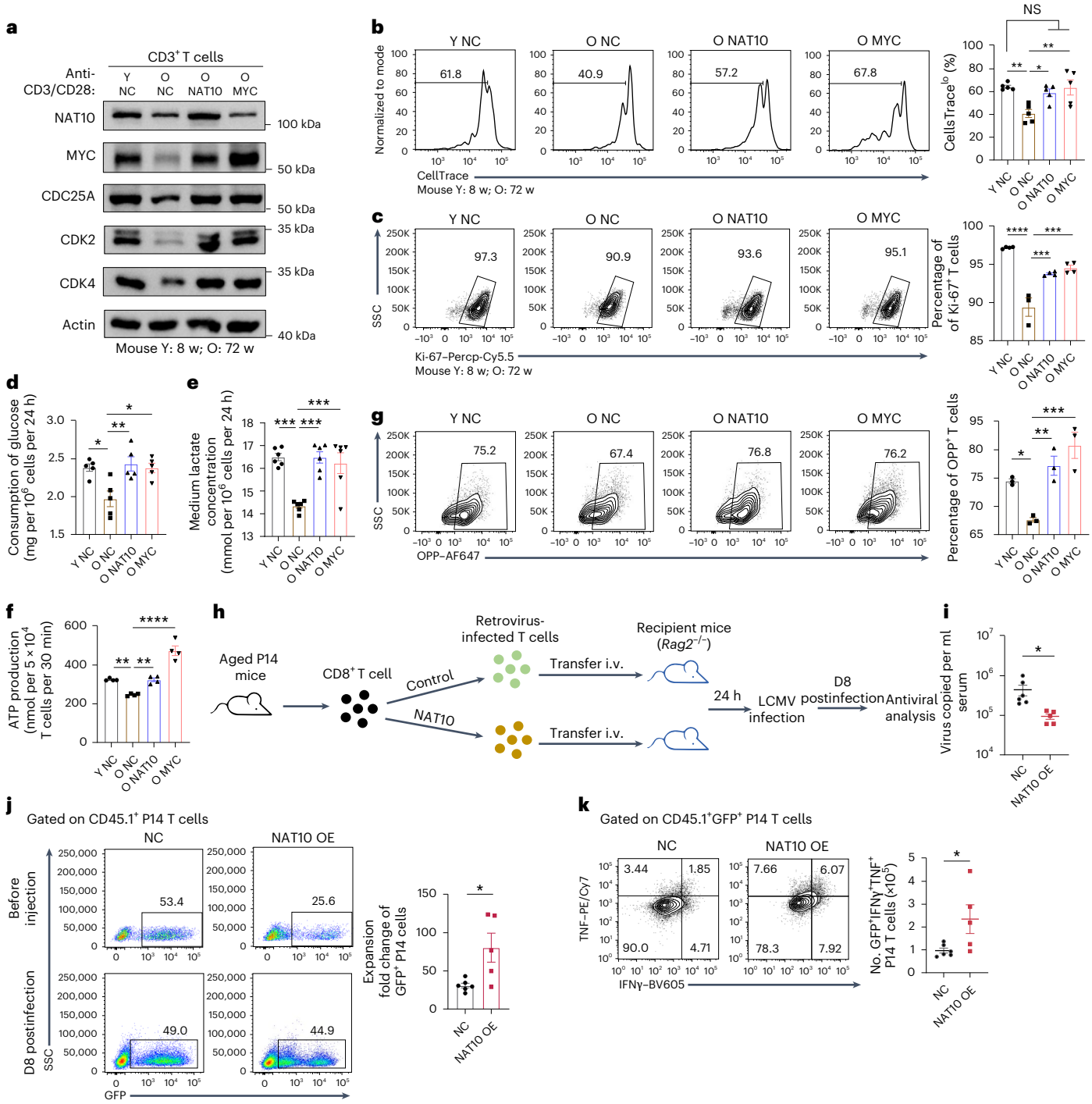

Fig. 8 | NAT10 overexpression restores proliferation and antiviral defects in T cells from older animals. a, NAT10 and MYC overexpression in T cells from aged mice. Representative data from three independent experiments are shown. Y, young; O, old; w, weeks. **b**,**c**, CellTrace dilution analysis (**b**) and Ki-67 expression (**c**) in T cells from aged mice with NAT10 or MYC overexpression. Left, representative flow plots. Right, bar diagrams showing the percentage of CellTrace^{lo} (**b**) or Ki-67^{+} (**c**) T cells in each group; $n = 5$ (**b**) and $n = 4$, 3, 4 and 4 (**c**). Exact P values from left to right: $^{**}P = 0.0052$, $^{*}P = 0.0315$ and $^{**}P = 0.0065$ (**b**) and $^{****}P < 0.0001$, $^{***}P = 0.0005$ and $^{***}P = 0.0001$ (**c**). **d**–**f**, Glucose consumption (**d**), lactate production (**e**) and ATP generation (**f**) in T cells from aged mice with NAT10 or MYC overexpression; $n = 5$, 6 and 4. Exact P values from left to right: $^{*}P = 0.0115$, $^{**}P = 0.0048$ and $^{*}P = 0.0122$ (**d**), $^{***}P = 0.0001$, $^{***}P = 0.0001$ and $^{***}P = 0.0006$ (**e**) and $^{**}P = 0.0081$, $^{**}P = 0.0086$ and $^{****}P < 0.0001$ (**f**). **g**, OPP staining of T cells from aged mice with NAT10 or MYC overexpression. Left, representative flow plots. Right, bar diagrams showing the percentage of OPP^{+} T cells in each group; $n = 3$; $^{***}P = 0.0010$, $^{**}P = 0.0073$ and $^{*}P = 0.0428$. **h**, Flow chart of experiments exploring the impact of NAT10 restoration on T cell antiviral potency. CD8^{+} T cells from old P14 mice with control or *Nat10*-overexpressing plasmids were transferred into 8-week-old *Rag2*$^{-/-}$ mice 1 day before LCMV infection. Eight days later, antiviral analysis was performed. **i**, Serum viral loads of recipients at 8 days after LCMV infection; NC $n = 6$, *Nat10* overexpression (OE) $n = 5$; $^{*}P = 0.0424$. **j**, Proportions of GFP^{+} P14 T cells in recipients. Left, representative flow plots. Right, bar diagrams showing the expansion fold changes of GFP^{+} P14 T cells in each group; NC $n = 6$, *Nat10* overexpression $n = 5$; $^{*}P = 0.0195$. **k**, Detection of IFNγ^{+}TNF^{+}GFP^{+} CD8^{+} T cells in recipients. Left, representative flow plots. Right, bar diagrams showing the absolute number of splenic IFNγ^{+}TNF^{+}GFP^{+} CD8^{+} T cells in the two groups; NC $n = 6$, *Nat10* overexpression $n = 5$; $^{*}P = 0.0415$. n refers to the number of biologically independent samples. Error bars represent mean ± s.e.m. (**b**–**g** and **i**–**k**). Data were analyzed by two-tailed, one-way ANOVA with a Tukey's multiple comparisons test (**b**–**g**) or two-tailed, unpaired t-test (**i**–**k**).

recovered age-induced compromised antiviral responses. Therefore, NAT10 might be another promising target for immunotherapy, especially in older individuals.

Discussion

Here, we present evidence that ac^{4}C functions as a form of epigenetic translational control, providing a crucial mechanism driving the rapid proliferation of activated T cells. Translation stands out as an active process in the early stages of T cell activation, and through the use of genetic mouse models, PBMC samples, high-throughput ac^{4}C RIP–seq, mRNA sequencing and Ribo-seq, the following key findings emerged: (1) expression of ac^{4}C proteins, particularly NAT10, undergoes a rapid increase following T cell activation within a very short timeframe; (2) TCR signaling activates NAT10-mediated ac^{4}C processing during T cell activation via c-JUN; (3) ac^{4}C modification acts as an essential translational checkpoint, stabilizing *Myc* mRNA and acting as a 'shield' for T cell activation and proliferation; and (4) diminished expression of NAT10 during aging is associated with the antiviral immunity of T cells.

Research efforts directed toward other epitranscriptomic modifications carry exemplary significance for furthering our understanding of ac^{4}C dynamics in this context[7,26,27]. When Arango et al. first identified NAT10 as the ac^{4}C writer, they described NAT10-deficient cells as highly viable, with reduced proliferation kinetics and a tendency for cell cycle arrest in the G2/M phase compared to WT control cells. Their sequencing data support this phenotype as genes altered after *Nat10* knockout were closely associated with cell survival and proliferation[28]. Later investigations further clarified the importance of NAT10 for cell division. Both mitosis of cancer cells[29] and meiosis of male germ cells[30] were found to be governed by NAT10-dependent machinery. Indeed, after deleting *Nat10* in T cells in vivo, we observed a marked shrinkage of the T cell pool in both immune (spleen and lymph nodes) and other parenchymatous organs (lung and kidney). Considering the extensive contraction of peripheral T cells in response to NAT10 deficiency, we speculate that the influence of ac^{4}C on T cells may largely situate in signaling pathways responding to environmental stimuli. It has also been extensively reported that NAT10-mediated ac^{4}C modification is involved in ribosome biogenesis[31,32]. In our scRNA-seq data, we also observe the same trend. However, in the context of this study, abnormal ribosomal protein expression may be attributed, in part, to impaired MYC expression because MYC is also a well-known regulator that promotes ribosome biogenesis[32,33].

Remarkably, despite ac^{4}C's emergence as a crucial aspect of epitranscriptomic regulation in RNA metabolism, its alterations at the tissue level during aging remain unexplored. In this study, we examined the ac^{4}C landscapes within the spleen and found a close association between age-related ac^{4}C loss and impaired T cell proliferation and differentiation. These findings suggest that the decrease in ac^{4}C modification observed during aging may contribute to T cell aging. However, given the multifactorial nature of immune senescence, it is important to acknowledge that ac^{4}C modifications likely operate alongside other regulatory mechanisms affecting immune functionality during aging. Further research is needed to clarify the interplay between these pathways. Considering the utility of DNA methylation in aging prediction[34], it would be equally intriguing to explore whether ac^{4}C modification could be harnessed to establish an aging biomarker in the future. Additionally, our observation of older individuals with COVID-19 harboring fewer proliferating T cells in response to infection with SARS-CoV-2 raises intriguing questions. Future studies should explore how NAT10 and ac^{4}C impact age-related antiviral immunity and the diminished ability to combat infections in greater detail. This study presents two key limitations that warrant further investigation. Specifically, (1) it is unclear what causes T cells to become hyperactive in the absence of NAT10, and (2) the regulation of T cells by NAT10 within the context of disease is intricate; therefore, it remains to be determined how NAT10 regulation interacts with COVID-19 severity and lymphopenia and whether they interfere with or support one another.

To date, whether this ac^{4}C writer protein participates in harnessing T cell development and function remains largely unknown. Here, we investigated the involvement of NAT10 in the maintenance of T cell expansion. Linked with the interesting observation that ac^{4}C modifications are decreased in individuals with systemic lupus erythematosus[4], our findings shed light on the crucial role of ac^{4}C mRNA modification in immune cell homeostasis and proliferation, opening avenues for exploiting the function of ac^{4}C in immune responses and immune deregulation.

Online content

Any methods, additional references, Nature Portfolio reporting summaries, source data, extended data, supplementary information, acknowledgements, peer review information; details of author contributions and competing interests; and statements of data and code availability are available at https://doi.org/10.1038/s41590-025-02100-2.

References

1. Wolf, T. et al. Dynamics in protein translation sustaining T cell preparedness. *Nat. Immunol.* **21**, 927–937 (2020).
2. Larrieu, D. et al. Inhibition of the acetyltransferase NAT10 normalizes progeric and aging cells by rebalancing the transportin-1 nuclear import pathway. *Sci. Signal.* **11**, eaar5401 (2018).
3. Tsai, K. et al. Acetylation of cytidine residues boosts HIV-1 gene expression by increasing viral RNA stability. *Cell Host Microbe* **28**, 306–312 (2020).
4. Guo, G. et al. Epitranscriptomic N^4-acetylcytidine profiling in CD4$^+$ T cells of systemic lupus erythematosus. *Front. Cell Dev. Biol.* **8**, 842 (2020).
5. Wang, K. et al. PIWI-interacting RNA HAAPIR regulates cardiomyocyte death after myocardial infarction by promoting NAT10-mediated ac^{4}C acetylation of *Tfec* mRNA. *Adv. Sci.* **9**, e2106058 (2022).
6. Yang, C. et al. Prognostic and immunological role of mRNA ac^{4}C regulator NAT10 in pan-cancer: new territory for cancer research? *Front. Oncol.* **11**, 630417 (2021).
7. Li, H. B. et al. m^{6}A mRNA methylation controls T cell homeostasis by targeting the IL-7/STAT5/SOCS pathways. *Nature* **548**, 338–342 (2017).
8. Durlanik, S. et al. CD40L expression by CD4$^+$ but not CD8$^+$ T cells regulates antiviral immune responses in acute LCMV infection in mice. *Eur. J. Immunol.* **46**, 2566–2573 (2016).
9. Oh, H. et al. An NF-κB transcription-factor-dependent lineage-specific transcriptional program promotes regulatory T cell identity and function. *Immunity* **47**, 450–465 (2017).
10. Martinez, G. J. et al. The transcription factor NFAT promotes exhaustion of activated CD8$^+$ T cells. *Immunity* **42**, 265–278 (2015).
11. Kurachi, M. et al. The transcription factor BATF operates as an essential differentiation checkpoint in early effector CD8$^+$ T cells. *Nat. Immunol.* **15**, 373–383 (2014).
12. Ciofani, M. et al. A validated regulatory network for T_H17 cell specification. *Cell* **151**, 289–303 (2012).
13. Singh, S., Vanden Broeck, A., Miller, L., Chaker-Margot, M. & Klinge, S. Nucleolar maturation of the human small subunit processome. *Science* **373**, eabj5338 (2021).
14. Gallagher, J. E. G. Proteins and RNA sequences required for the transition of the t-Utp complex into the SSU processome. *FEMS Yeast Res.* **19**, foy120 (2019).
15. Jin, G., Xu, M., Zou, M. & Duan, S. The processing, gene regulation, biological functions, and clinical relevance of N^4-acetylcytidine on RNA: a systematic review. *Mol. Ther. Nucleic Acids* **20**, 13–24 (2020).

16. Min, B. Spontaneous T cell proliferation: a physiologic process to create and maintain homeostatic balance and diversity of the immune system. *Front. Immunol.* **9**, 547 (2018).
17. Wagner, A. et al. Metabolic modeling of single T_H17 cells reveals regulators of autoimmunity. *Cell* **184**, 4168–4185 (2021).
18. El Chakhtoura, N. G., Bonomo, R. A. & Jump, R. L. P. Influence of aging and environment on presentation of infection in older adults. *Infect. Dis. Clin. North. Am.* **31**, 593–608 (2017).
19. Overmyer, K. A. et al. Large-scale multi-omic analysis of COVID-19 severity. *Cell Syst.* **12**, 23–40 (2021).
20. Oliveira, T. T., Freitas, J. F., de Medeiros, V. P. B., Xavier, T. & Agnez-Lima, L. F. Integrated analysis of RNA-seq datasets reveals novel targets and regulators of COVID-19 severity. *Life Sci. Alliance* **7**, e202302358 (2024).
21. Shen, X. R. et al. ACE2-independent infection of T lymphocytes by SARS-CoV-2. *Signal Transduct. Target. Ther.* **7**, 83 (2022).
22. Wilk, A. J. et al. Multi-omic profiling reveals widespread dysregulation of innate immunity and hematopoiesis in COVID-19. *J. Exp. Med.* **218**, e20210582 (2021).
23. Diao, B. et al. Reduction and functional exhaustion of T cells in patients with coronavirus disease 2019 (COVID-19). *Front. Immunol.* **11**, 827 (2020).
24. Sheu, T. T. & Chiang, B. L. Lymphopenia, lymphopenia-induced proliferation, and autoimmunity. *Int. J. Mol. Sci.* **22**, 4152 (2021).
25. Ren, X. et al. COVID-19 immune features revealed by a large-scale single-cell transcriptome atlas. *Cell* **184**, 1895–1913 (2021).
26. Liu, Y. et al. tRNA-m^1A modification promotes T cell expansion via efficient MYC protein synthesis. *Nat. Immunol.* **23**, 1433–1444 (2022).
27. Yang, W. L. et al. Nsun2 coupling with RoRγt shapes the fate of T_H17 cells and promotes colitis. *Nat. Commun.* **14**, 863 (2023).
28. Arango, D. et al. Acetylation of cytidine in mRNA promotes translation efficiency. *Cell* **175**, 1872–1886 (2018).
29. Zheng, J. et al. NAT10 regulates mitotic cell fate by acetylating Eg5 to control bipolar spindle assembly and chromosome segregation. *Cell Death Differ.* **29**, 846–860 (2022).
30. Chen, L. et al. NAT10-mediated N^4-acetylcytidine modification is required for meiosis entry and progression in male germ cells. *Nucleic Acids Res.* **50**, 10896–10913 (2022).
31. Ito, S. et al. Human NAT10 is an ATP-dependent RNA acetyltransferase responsible for N^4-acetylcytidine formation in 18S ribosomal RNA (rRNA). *J. Biol. Chem.* **289**, 35724–35730 (2014).
32. Chan, J. C. et al. AKT promotes rRNA synthesis and cooperates with c-MYC to stimulate ribosome biogenesis in cancer. *Sci. Signal.* **4**, ra56 (2011).
33. Tan, T. C. J. et al. Suboptimal T-cell receptor signaling compromises protein translation, ribosome biogenesis, and proliferation of mouse CD8 T cells. *Proc. Natl Acad. Sci. USA* **114**, E6117–E6126 (2017).
34. Wu, Z. et al. m^6A epitranscriptomic regulation of tissue homeostasis during primate aging. *Nat. Aging* **3**, 705–721 (2023).

Publisher's note Springer Nature remains neutral with regard to jurisdictional claims in published maps and institutional affiliations.

Open Access This article is licensed under a Creative Commons Attribution-NonCommercial-NoDerivatives 4.0 International License, which permits any non-commercial use, sharing, distribution and reproduction in any medium or format, as long as you give appropriate credit to the original author(s) and the source, provide a link to the Creative Commons licence, and indicate if you modified the licensed material. You do not have permission under this licence to share adapted material derived from this article or parts of it. The images or other third party material in this article are included in the article's Creative Commons licence, unless indicated otherwise in a credit line to the material. If material is not included in the article's Creative Commons licence and your intended use is not permitted by statutory regulation or exceeds the permitted use, you will need to obtain permission directly from the copyright holder. To view a copy of this licence, visit http://creativecommons.org/licenses/by-nc-nd/4.0/.

© The Author(s) 2025

Methods

Human samples

In this study, PBMCs were isolated from the blood of healthy donors and used to perform FCM or western blotting. All participants were recruited from Jinshan Hospital with written informed consent. The study was approved by the Ethics Committee of Jinshan Hospital (JIEC 2023-S47). Healthy donors were defined as (1) aged 18–85 years old, (2) no infectious diseases over the past 6 months, (3) no malignant tumor history and (4) no history of autoimmune disease. Routine blood examinations were performed to ensure the quality and eligibility of each donor. Samples from a total of six men and four women were collected, with 2–3 ml whole blood obtained from each participant.

Mice

Six- to 8-week-old C57BL/6J WT mice were purchased from SPF Biotechnology. Seventy-two-week-old C57BL/6J mice were purchased from Jiangsu Huachuang Sino Pharma Tech. FLOX mice were gifted from Y. Lu (Shanghai Jiao Tong University). *Cd4*^{Cre} mice were purchased from Cyagen Biosciences. To generate *Nat10*-CKO mice, FLOX mice were crossed with *Cd4*^{Cre} mice. P14 mice were a gift from the laboratory of L. Ye (Army Medical University). *Rag2*$^{-/-}$ mice were purchased from Cyagen Biosciences. Mice were housed and routinely handled in Cyagen Biosciences and Shanghai Public Health Clinical Center under specific pathogen-free conditions following institutional guidelines. All mice were fed with standard mice chow (specific pathogen free, SPF-F02-002). Animal procedures were reviewed and approved by the Institutional Animal Care and Use Committee of Shanghai Public Health Clinical Center (2023-A053-01).

T cell isolation and culture

Naive or total CD3$^+$ T cells were purified using an EasySep Mouse Naive T Cell Isolation kit (STEMCELL Technologies) or a MojoSort Mouse CD3 T Cell Isolation kit (Biolegend) according to the respective instructions. In vitro-activated CD3$^+$ T cells were generated by stimulating naive CD3$^+$ T cells with plate-bound anti-CD3ε (Biolegend, clone 2C11; 5 μg ml^{-1}) and dissolvable anti-CD28 (eBioscience, clone 37.51; 0.5 μg ml^{-1}) in the presence of IL-2 (PeproTech; 100 U ml^{-1}). Naive CD3$^+$ T cells labeled with CFSE (BD Pharmingen) or CellTrace (Thermo Fisher Scientific) were stimulated for 72 h. CFSE or CellTrace dilutions were used to assess cell proliferation. For cell cycle analysis, naive CD3$^+$ T cells were stimulated for 48 h, followed by BrdU/7-AAD double staining using a FITC BrdU Flow kit (BD Pharmingen), as per the manufacturer's protocol. For RNA-seq and ac^{4}C RIP–seq, cells were washed twice after 72 h of stimulation, transferred to a new plate and cultured for another 3 days in the presence of 100 U ml^{-1} IL-2 only to obtain enough activated T cells. The medium used contained RPMI-1640, 10% fetal bovine serum (Gibco), 2 mM L-glutamine (Gibco), 1 mM sodium pyruvate (Sigma-Aldrich), 10 mM HEPES (Sigma-Aldrich) and 50 μM β-mercaptoethanol (Sigma-Aldrich).

Human PBMC isolation and culture

Human PBMCs were isolated by Ficoll gradient centrifugation of fresh blood as previously described[35]. The PBMCs were seeded into 24-well plates and stimulated with plate-bound anti-CD3ε (Biolegend, clone OKT3; 5 μg ml^{-1}) and dissolvable anti-CD28 (Biolegend, clone CD28.2; 1 μg ml^{-1}) in the presence of human recombinant IL-2 (PeproTech; 200 U ml^{-1}). After 48 h, cells were collected for FCM and western blotting. The medium used in this culture system contained X-VIVO-15 serum-free hematopoietic cell medium and 5% fetal bovine serum.

LCMV infection

LCMV Armstrong strain was a gift from L. Ye. Virus was propagated, and titers were measured as previously described[36]. Mice were intraperitoneally injected with 2 × 10^5 p.f.u. virus to establish an acute infection.

For the adaptive transfer model, 2 × 10^5 P14 T cells transfected with control or *Nat10*-overexpressing plasmids were transferred to *Rag2*$^{-/-}$ recipients, respectively. A total of 4 × 10^5 p.f.u. LCMV Armstrong was administrated to each recipient 24 h later, and 4 × 10^5 P14 T cells with *Nat10* knockdown and their negative controls were transfected into WT mice 1 day before constructing the acute LCMV infection model. Seven to 8 days later, recipients were killed for further analysis.

Viral load measured by real-time qPCR

RNA was extracted from 140 μl of serum using a QIAamp Viral RNA Mini kit (Qiagen). Measurement of viral load by real-time qPCR was performed as previously described[37]. cDNA was synthesized by using PrimeScript RT Master Mix (Takara). qPCR was performed with Premix Ex Taq (Takara) following the manufacturer's instructions. Standard curves were generated using serial dilutions of a plasmid template containing a 411-bp gene fragment derived from Armstrong NP open reading frames. Probe, primer and fragment template sequences are available in Supplementary Table 4.

Sample preparation and FCM

Spleen, thymus, lymph node, lung, kidney and liver tissue were collected and ground through 70-μm filters (WHB Scientific). Erythrocytes were lysed with red blood cell lysis buffer (Solarbio), and remaining cells isolated by centrifugation were stained for subsequent FCM analysis. For viability staining, cells were stained with Fixable Viability Stain 510 (BD Pharmingen) in PBS (1:600) at room temperature for 15 min. For cell surface staining, cells were stained with antibodies in cell staining buffer (1:200) at 4 °C for 30 min. For intracellular staining, cells were treated with phorbol 12-myristate 13-acetate/ionomycin (BioLegend) for 5 h at 37 °C, and intracellular cytokine staining was performed using a Transcription Factor Buffer Set (BD Pharmingen) according to manufacturer's recommendations. Notably, when it comes to functionality detection of T cells from LCMV-infected mice, cells were incubated with GP_{33-41} peptide (2 μg ml^{-1}; Absin) in the presence of brefeldin and monensin. Absolute counts for lymphocytes were calculated based on FCM gating and total number of splenic or lymph node cells. Apoptosis assays were performed with a FITC Annexin V Apoptosis Detection Kit I (BD Pharmingen) according to the manufacturer's instructions. For cell cycle analysis, BrdU/7-AAD double staining was performed with a FITC BrdU Flow kit (BD Pharmingen), as per the manufacturer's protocol. Samples were acquired on a BD FACSLyric Cytometer. All data analysis was performed using FlowJo 10.4 software (FlowJo). Sorting assays were performed using a FACS Aria Cytometer (BD Bioscience). Gating strategies are presented in Extended Data Fig. 7.

In vivo T cell proliferation assay

In this study, we used CellTrace dyes to monitor cell proliferation and division by FCM. Naive CD3$^+$ T cells from FLOX (CD45.1$^+$) and CKO mice (CD45.2$^+$) were purified as described above, labeled with CellTrace (Thermo) and mixed at a 1:1 ratio. One million cells were then transferred into each *Rag2*$^{-/-}$ recipient mouse intravenously. CellTrace dilution of donor cells in recipients was assessed before and 96 h after transfer by FCM.

NAT10/MYC overexpression in vivo

Bone marrow chimeric mouse models were constructed as previously described[38]. Briefly, FLOX and CKO donors (CD45.2$^+$) were intraperitoneally administrated with 5-fluorouracil (Sigma-Aldrich) prepared in PBS at a dose of 150 mg per kg (body weight). After 24 h, HSCs were enriched from bone marrow cells with a CD117$^+$ selection kit (Stem Cell Technologies) and then incubated with retroviral supernatants containing MIGR1 plasmids for spin infection, as previously described. During HSC transfection, recipient mice (CD45.1$^+$) were sublethally irradiated

(9 Gy), and protectors were collected from untreated normal mice ($CD45.1^+CD45.2^+$). HSCs and protectors were then both suspended to 5×10^6 cells per ml and mixed at a 1:1 ratio. Next, each recipient was intravenously administered with 0.2 ml of cell suspension (total of 1 million cells). The proliferation status of CKO T cells with control or *Nat10*- or *Myc*-overexpressing plasmids was assessed compared to FLOX control mice 10 weeks later.

Metabolomics profiling

Q300 service was provided by Metabo-Profile Biotechnology. Naive and 24-h-activated $CD3^+$ T cells were collected and stored in microcentrifuge tubes. Absolute quantification of intracellular metabolites was performed using a Q300 kit (Metabo-Profile) as previously described[39]. Briefly, cells were homogenized using ten zirconium oxide beads with 20 µl of deionized water. After methanol (150 µl) containing internal standard was added, the samples were homogenized for the second time and centrifuged at 18,000*g* for 20 min. The supernatants were then transferred to a 96-well plate, mixed with 20 µl of newly prepared derivative reagents for further derivatization at 30 °C for 60 min and evaporated for 2 h. After that, the samples were diluted with 330 µl of ice-cold 50% methanol, held at −20 °C for 20 min and centrifuged at 4,000*g* at 4 °C for 30 min. In total, 135 µl of supernatant with 10 µl of internal standards per sample was transferred into a new 96-well plate. Serial dilutions of the standard were added, and the plate was sealed for further LC–MS/MS analysis. All of the standards (Sigma-Aldrich, Steraloids, TRC Chemicals) were accurately weighed and prepared in appropriate solvents to obtain a 5 mg ml^{-1} stock solution. As for instrumentation, a UPLC–MS/MS system (Acquity UPLC-Xevo TQ-S, Waters) was used to quantify the targeted metabolites. For data processing, the raw data were processed via the iMAP platform (v1.0; Metabo-Profile)[40]. Contents of detected metabolites are displayed in Supplementary Table 1.

Targeted quantification of nucleotides was also performed by Metabo-Profile Biotechnology. Naive and 24-h-activated $CD3^+$ T cells were collected and stored in microcentrifuge tubes. Each sample was combined with 200 µl of precooled 80% methanol–water and crushed by ultrasound three times at 2% power for 5 s (JY92-IIN, NingBo Scientz Biotechnology). Centrifugation was performed at 4 °C at 18,000*g* for 20 min (Microfuge 20R, Beckman Coulter). Sixty microliters of supernatant from each sample was transferred to the sample bottle and awaited sample loading. Blank control samples and quality control samples were treated similarly. Serial dilutions of the standard were also added into the plate for further LC–MS/MS analysis. All of the standards (Sigma-Aldrich, Steraloids, TRC Chemicals) were accurately weighed and prepared in appropriate solvents to obtain 5 mg ml^{-1} stock solutions. For instrumentation, a UPLC–MS/MS system (Acquity UPLC-Xevo TQ-S, Waters) was used to quantify nucleotides in each sample. For data processing, the raw data were processed with MassLynx software (v4.1; Waters) and analyzed on an iMAP platform (v1.0; Metabo-Profile). Contents of detected nucleotides are displayed in Supplementary Table 2.

Glucose uptake measurements

T_N cells were purified from 8-week-old FLOX and CKO mice, with anti-CD3/CD28 stimulation for 24 h. After being incubated with glucose-free RPMI-1640 containing 10% fetal bovine serum (Gibco) for 4 h, cells were then treated with 2-NBDG for 30 min. Glucose uptake was assessed by FITC fluorescence intensity via FCM detection. For CKO and T cells from aged mice with NAT10 overexpression, glucose consumption was measured to replace the 2-NBDG for the conflicted fluorescence color. Briefly, 1×10^6 T cells were suspended with 1 ml of fresh complete medium and cultured as normal. One milliliter of medium without T cells was used as a blank control. Twenty-four hours later, the culture medium of each group was collected for glucose content detection by using a Glucose Assay kit (Beyotime). Glucose consumption could then be calculated as the difference between the samples and blank controls.

Metabolism assays

Real-time cell metabolic flux analysis was performed on an XF-96 Extracellular Flux Analyzer (Seahorse Bioscience). A total of 5×10^5 FLOX or CKO T cells were plated into each well of a culture microplate and incubated at 37 °C for 1 h in the absence of CO_2 in unbuffered RPMI with 1% bovine serum, 1 mM pyruvate, 2 mM L-glutamine and 10 mM glucose. Half of the cells in each group were supplemented with an equal amount of anti-CD3/CD28 beads (5×10^5 cells per well). ECAR and OCR were then measured under basal conditions.

ATP measurements

T_N cells were purified from 8-week-old FLOX and CKO mice, some of which were stimulated with anti-CD3/CD28 for 24 h. ATP production in FLOX-T_N, CKO-T_N, FLOX-T_{EFF} and CKO T_{EFF} cells was measured using an ATPlite 1step Luminescence Assay (PerkinElmer), as per the manufacturer's instructions.

Protein synthesis assays

Cells were prepared according to experimental targets. OPP staining and detection were then performed using a Click-iT Plus OPP Alexa Fluor 647 Protein Synthesis Assay kit (Thermo) as per the manufacturer's instructions.

Lactate production measurements

T cells (1×10^6) were suspended with 1 ml of fresh complete medium and cultured as normal. One milliliter of medium without T cells was used as a blank control. Twenty-four hours later, the culture medium of each group was collected for lactate content detection. Lactate production could then be detected using a CheKine Micro Lactate Assay kit (Abbkine) following the manufacturer's instructions.

RNA ac^4C dot blot

Purified RNA diluted to the indicated concentrations was incubated at 95 °C for 3 min, and equal volumes of RNA samples were transferred onto two nitrocellulose membranes, respectively. After air drying for 20 min, the RNA samples were cross-linked to the membranes by UV radiation with a dose of 5 J three times. One membrane was incubated with methylene blue (0.02% in 0.3 M sodium acetate) and washed with double-distilled water for 1 h to obtain the loading control. The other membrane was blocked with 5% bovine serum albumin and incubated with anti-ac^4C (Abcam) overnight at 4 °C, followed by incubation with secondary antibody (Proteintech) for 90 min at room temperature. Finally, blot signals were detected using a ChemiScope 6100 (Clinx Science Instruments). Densitometry analysis was performed using ImageJ v.1.53a software.

RIP–qPCR

The ac^4C RIP assay was performed using a GenSeq ac^4C RIP kit (GS-ET-005, Cloudseq Biotech) as per the manufacturer's instructions. In detail, total RNA (100 µg) was randomly digested into 100- to 200-bp fragments and incubated with a mixture of 5 µg of anti-ac^4C or IgG and magnetic beads. Anti-ac^4C-bound RNAs were purified, and enrichment of *Myc* mRNA was determined by qPCR with reverse transcription. For the NAT10 RIP assay, primary anti-ac^4C was replaced with anti-NAT10, with the other procedures unchanged. The primers used are listed in the Supplementary Table 4.

ChIP–qPCR

WT naive $CD3^+$ T cells were isolated and stimulated with anti-CD3/CD28 for 24 h. The ChIP assay was performed using a ChIP assay kit (Cell Signaling Technology). qPCR was then conducted to confirm c-JUN binding to *Nat10* loci. The primers used are listed in Supplementary Table 4.

RNA degradation assay

Naive $CD3^+$ T cells were isolated and stimulated as previously described for 24 h and then treated with 2.5 μg ml^{-1} actinomycin D for 0, 1 and 2 h. Total cellular RNA was then collected. The relative transcriptional expression of *Myc* was determined by qPCR with reverse transcription.

Ribo-seq

Ribo-seq was provided by CloudSeq Biotech. Isolated $CD3^+$ FLOX and CKO T cells were mixed with medium containing 0.1 mg ml^{-1} cycloheximide (Sigma-Aldrich) softly and centrifuged at 200*g* for 5 min. After supernatants were removed, cells were resuspended with prechilled PBS containing 0.1 mg ml^{-1} cycloheximide and transferred to prechilled microcentrifuge tubes, followed by another centrifugation. T cells were then lysed using lysis buffer (10 mM HEPES-KOH (pH 7.4), 150 mM KCl, 10 mM $MgCl_2$, 1 mM DTT, 100 μg ml^{-1} cycloheximide and 2% NP-40), and cell lysates were digested by RNase I to obtain RPFs. After rRNA removal using a Ribo-zero kit (Illumina), a repertoire of short RPFs (20–38 nucleotides) were purified by PAGE. 5′ starts and 3′ ends of the RPFs were subsequently phosphorylated and ligated to adapters. cDNA synthesized via reverse transcription was PAGE purified again and amplified by PCR to prepare initial libraries. After PAGE purification for the third time, the cDNA libraries containing 140- to 160-bp fragments were subjected to an Illumina NovaSeq 6000 instrument for sequencing. For data analysis, filtered clean reads were aligned to the reference genome (UCSC hg19) using TopHat2 software[41]. The number of reads was counted using HTSeq[42], and differentially expressed genes were analyzed using DESeq2 software[43], with a cutoff of an adjusted *P* value of <0.05 and $|\log_2(\text{fold change})|$ of >1.

Polyribosome real-time PCR

Naive $CD3^+$ T cells were isolated from FLOX and CKO mice, activated as previously described for 24 h and then incubated with cycloheximide (100 μg ml^{-1}; Med Chem Express) for 5 min. Cells were then collected and washed with prechilled PBS (containing 100 μg ml^{-1} cycloheximide). After lysis, one-third of the lysate was set aside as input, and the remainder was gently added to the sucrose gradient buffer, followed by centrifugation at 274,000*g* for 1.5 h at 4 °C. Gradient fractions were then collected via Biocomp Piston Gradient Fractionator. RNase inhibitor (Beyotime) was added to the entire liquid system at a final concentration of 1,000 U ml^{-1}. RNAs from polyribosome fractions and input were purified with an RNA Clean & Concentrator kit (Zymo Research) for further qPCR analysis.

Plasmid construction, virus production and virus infection

The *Nat10* overexpression plasmid and *Myc* overexpression plasmid were constructed based on retroviral vectors pMXs-IRES-GFP (a gift from J. Jin, Fudan University) or MIGR1-IRES-GFP (a gift from H. Hu, Sichuan University) via homologous recombination. The *Nat10*-knockdown plasmid was built from LMP-IRES-AmCyan (a gift from J. Jin). A ClonExpress II One Step Cloning kit (Vazyme), 2× Phanta Max Master Mix (Vazyme) and Trellef DNA Gel Extraction kit (safe & convenient; Tsingke) were used in this procedure. Plasmids were sequence confirmed by Sanger sequencing (Genewiz) and amplified using DH5α competent cells (Tsingke). To generate retroviral particles, Plat E (a gift from J. Jin, for pMXs and LMP plasmids) or 293T cells (for MIGR1 plasmids) were transfected with plasmids along with Lipo6000 (Beyotime). Forty-eight hours later, supernatants including 10 μg ml^{-1} Polybrene (Beyotime) were filtered and mixed with prepared T cells or HSCs. The mixtures were then spun at 800*g* for 2 h at 33 °C and left undisturbed for 3 h in an incubator at 37 °C. Cells were then moved to fresh culture medium or were collected for subsequent treatments. Successfully infected cells were distinguished by fluorescence via FCM.

acRIP–seq

The acRIP-Seq service was supported by CloudSeq Biotech. Total RNA was extracted from flow-sorted FLOX and CKO T_{EFF} cells, with rRNA removed using a Ribo-zero kit (Illumina). ac^4C-IP was then performed using a GenSeq ac^4C-IP kit (GenSeq), as per the manufacturer's instructions. Briefly, RNA was fragmented into pieces smaller than 200 nucleotides with RNA fragmentation reagents. Protein A/G beads were conjugated to anti-ac^4C via incubation with gentle rotation at room temperature for 1 h. Fragmented RNA samples were incubated with the antibody-prebound beads with rotation at 4 °C for 4 h. IPs were then treated with Proteinase K, and the eluted RNA was recovered by phenol/chloroform extraction. RNA libraries were then constructed with an NEBNext Ultra II Directional RNA Library Prep kit (New England Biolabs) according to the manufacturer's instructions. Newly established libraries were checked using an Agilent BioAnalyzer 2100 system and sequenced on the NovaSeq platform (Illumina). Raw sequencing reads from an Illumina NovaSeq 6000 sequencer were quality controlled by Q30 and processed with Cutadapt software[44] (v1.9.3) to trim the 3′ adaptor and remove low-quality alignments. The filtered clean reads were then aligned to the reference genome with HISAT2 software (v2.0.4)[45]. ac^4C-enriched regions (peaks) were identified by MACS software[46], and differentially acetylated sites were identified with diffReps[47]. The peaks pinpointed earlier that overlapped with exons were identified and chosen by in-house scripts. Genomic distributions of ac^4C peaks were visualized using IGV. Motif analysis was performed with the Discriminative Regular Expression Motif Elicitation software according to the default workflow. The metaPlotR package helped to perform the metagene analysis of ac^4C sites identified on mRNAs from FLOX and CKO T_{EFF} cells[48].

RNA-seq and analysis

In this study, the RNA-seq service was supported by CloudSeq Biotech. Samples of mouse spleen and liver tissues and $CD3^+$ T_N and T_{EFF} cells were prepared, and total RNA was extracted. rRNA was removed using an NEBNext rRNA Depletion kit (New England Biolabs) according to the manufacturer's instructions. RNA libraries were then constructed with an NEBNext Ultra II Directional RNA Library Prep kit (New England Biolabs) following the manufacturer's instructions. After quality control and quantification on a BioAnalyzer 2100 system (Agilent Technologies), libraries were sequenced on an Illumina NovaSeq 6000 instrument with paired end reads of 150 bp. After quality control by Q30, the raw data were further filtered via 3′ adaptor trimming using cutadapt software (v1.9.3)[44] to obtain high-quality clean reads, which were mapped to the reference genome (UCSC MM10) using HISAT2 software (v2.0.4). HTSeq software (v0.9.1) was then used to generate the raw count, and the edgeR[49] package was used to perform normalization and examine differentially expressed genes with a $|\log_2(\text{fold change})|$ of ≥ 1 and false discovery rate of ≤0.05. GO and pathway enrichment analysis was performed using the clusterProfiler package[49,50]. GSEA was performed using the R package AUCell[51]. For combined analysis, ac^4C^+ and ac^4C^- mRNAs were first picked according to acRIP–seq. The ggplots package was then used to calculate the differential expression between the two groups to generate cumulative distribution function plots or within each group to generate volcano plots. For RNA-seq data from individuals with COVID-19, gene expression matrixes were obtained from the Gene Expression Omnibus (GEO) database and processed in the R programming environment. Transcripts per million (TPM) values were transformed using log (TPM + 1) for expression comparison. Box plots were generated using the ggplot2 package, with statistical significance calculated using the stat_compare_means function (*t*-test)[52]. The ggpubr package was then used for correlation analyses[53]. ChIP–seq data were downloaded from the GEO database in SRA format and converted to FASTQ format in the Linux system with the Conda environment using parallel-fastq-dump software. After quality control, the cleaned files were then aligned to the mouse

reference genome (mm10) using bowtie2, generating alignment results in SAM format.

The alignment files were further converted to BAM format using samtools. MACS2 software was then used to perform peak calling and identify potential binding regions in the genome. The resulting files from MACS2 were converted into BigWig format using the bedGraphToBigWig tool. IGV software was used for visualization.

scRNA-seq, clustering and analysis

scRNA-seq was performed by Sinotech Genomics. Spleen and thymus tissue collected from FLOX and CKO mice were ground into single-cell suspensions and filtered through 40-µm cell strainers. Cells were then double stained with Calcein AM and Draq7 to determine cell concentration and viability using a BD Rhapsody Scanner (BD Biosciences). The BD Rhapsody system was used to capture cells in microwells. After treatment with lysis buffer, microbeads that captured cells were retrieved, washed and subjected to reverse transcription. cDNA libraries were generated based on the acquired single-cell transcriptome. A BD Rhapsody cDNA kit (BD Biosciences) and BD Rhapsody Targeted mRNA & AbSeq Amplification kit (BD Biosciences) were used to capture single-cell transcriptomes and construct libraries. All sequencing procedures were performed on an Illumina NovaSeq platform. Raw data were processed and aligned to Genome Reference Consortium Mouse Build 39 (GRCm39) using the BD Rhapsody Whole Transcriptome Assay Analysis Pipeline (v1.8). Seurat[54] was used for clustering analysis and visualization. Dimensionality reduction analysis was performed using *t*-SNE or UMAP with a resolution of 0.6 (ref. 55). Specific marker genes of each cluster were assessed using the FindAllMarkers function with a Wilcoxon test, and SingleR was used to identity cell type. Compass was applied to visualize cellular metabolic states based on scRNA-seq data[17].

For single-cell transcriptomic data of PBMCs from individuals with COVID-19, the Seurat package was used for preprocessing, followed by batch effect correction and data integration using the harmony function[54]. Dimensionality reduction and clustering were performed using the UMAP method[55]. The DotPlot function was used to generate bubble plots depicting the expression of *NAT10* across different cell subpopulations. After calculating the proportion of $CD8^+$ proliferative T cells, box plots were generated using the ggplot2 package, and statistical significance was assessed with the stat_compare_means function (*t*-test)[52].

RNA extraction and real-time qPCR

Total RNA was purified with an RNA-Quick Purification kit (ES Science). One microgram of total RNA was reverse transcribed using SYBR Premix Ex Taq II (Takara). Diluted cDNA samples were then subjected to quantitative real-time PCR analysis using SYBR Premix Ex Taq II (Takara), following the manufacturer's instructions, on a StepOnePlus Real-Time PCR System. *GAPDH* was used as endogenous normalization control. Primers for *MYC* were synthesized at Sangon Biotech, and specific sequences are available in Supplementary Table 4.

Western blotting

Collected cells and tissues were lysed in RIPA buffer (Beyotime) on ice for 30 min, with protease and phosphatase inhibitors (Beyotime) added. Lysates were centrifuged at 12,000*g* for 5 min at 4 °C to obtain the supernatant. Protein content was then quantified by bicinchoninic acid assay (Beyotime) and diluted to a final concentration of 1–2 µg $µl^{-1}$. After the addition of 5× SDS–PAGE loading buffer (Beyotime), samples were boiled at 100 °C for 10 min, resolved via SDS–PAGE and transferred to a PVDF membrane (Millipore). Membranes were blocked in 5% skim milk at room temperature for 1 h and subsequently incubated with the indicated primary and secondary antibodies. Blot signals were detected using a ChemiScope 6100 (Clinx Science Instruments).

Statistical analysis

All experiments were performed with at least three biological replicates. GraphPad Prism 9.0.0 was used for statistical analyses. No data were excluded from the reported analyses. Data distribution was assumed to be normal, with no normality tests performed. Detailed statistical descriptions, including sample size and calculation methods, are provided in the figure legends.

Reporting summary

Further information on research design is available in the Nature Portfolio Reporting Summary linked to this article.

Data availability

Bulk RNA-seq and acRIP–seq data in this study were deposited in the Genome Sequence Archive (GSA) under accession numbers CRA015058, CRA015065, CRA015132 and CRA015079. scRNA-seq data were uploaded to the GSA under accession number CRA015122. ChIP–seq data are accessible from GEO under the following accession numbers: GSE99319, GSE64409, GSE54191 and GSE40918. Raw metabolomics data were deposited in the MetaboLights database under accession numbers MTBLS9639 and MTBLS9640. Quantitative metabolite information is available in Supplementary Tables 1 and 2. Processed scRNA-seq data from individuals with COVID-19 provided by the laboratory of C. A. Blish (Stanford University School of Medicine) are available from the COVID-19 Cell Atlas (https://www.covid19cellatlas.org/). RNA-seq data from leukocytes derived from individuals with COVID-19 are available from GEO under accession number GSE157103. Source data are provided with this paper.

Code availability

All code used in this study is included in other published studies and is cited in the Methods. No new code for statistical analysis was developed.

References

35. Kizhakeyil, A. et al. Isolation of human peripheral blood T-lymphocytes. *Methods Mol. Biol.* **1930**, 11–17 (2019).
36. Dangi, T., Chung, Y. R., Palacio, N. & Penaloza-MacMaster, P. Interrogating adaptive immunity using LCMV. *Curr. Protoc. Immunol.* **130**, e99 (2020).
37. McCausland, M. M. & Crotty, S. Quantitative PCR technique for detecting lymphocytic choriomeningitis virus in vivo. *J. Virol. Methods* **147**, 167–176 (2008).
38. Qi, Z. et al. SRSF1 serves as a critical posttranscriptional regulator at the late stage of thymocyte development. *Sci. Adv.* **7**, eabf0753 (2021).
39. Xie, G. et al. A metabolite array technology for precision medicine. *Anal. Chem.* **93**, 5709–5717 (2021).
40. Zhou, D. et al. iMAP: a web server for metabolomics data integrative analysis. *Front. Chem.* **9**, 659656 (2021).
41. Kim, D. et al. TopHat2: accurate alignment of transcriptomes in the presence of insertions, deletions and gene fusions. *Genome Biol.* **14**, R36 (2013).
42. Anders, S., Pyl, P. T. & Huber, W. HTSeq—a Python framework to work with high-throughput sequencing data. *Bioinformatics* **31**, 166–169 (2015).
43. Love, M. I., Huber, W. & Anders, S. Moderated estimation of fold change and dispersion for RNA-seq data with DESeq2. *Genome Biol.* **15**, 550 (2014).
44. Martin, M. Cutadapt removes adapter sequences from high-throughput sequencing reads. *EMBnet.journal* **17**, 10–12 (2011).
45. Kim, D., Langmead, B. & Salzberg, S. L. HISAT: a fast spliced aligner with low memory requirements. *Nat. Methods* **12**, 357–360 (2015).
46. Zhang, Y. et al. Model-based analysis of ChIP–seq (MACS). *Genome Biol.* **9**, R137 (2008).

47. Shen, L. et al. diffReps: detecting differential chromatin modification sites from ChIP–seq data with biological replicates. *PLoS ONE* **8**, e65598 (2013).
48. Olarerin-George, A. O. & Jaffrey, S. R. MetaPlotR: a Perl/R pipeline for plotting metagenes of nucleotide modifications and other transcriptomic sites. *Bioinformatics* **33**, 1563–1564 (2017).
49. Robinson, M. D., McCarthy, D. J. & Smyth, G. K. edgeR: a Bioconductor package for differential expression analysis of digital gene expression data. *Bioinformatics* **26**, 139–140 (2010).
50. Yu, G., Wang, L. G., Han, Y. & He, Q. Y. clusterProfiler: an R package for comparing biological themes among gene clusters. *OMICS* **16**, 284–287 (2012).
51. Aibar, S. et al. SCENIC: single-cell regulatory network inference and clustering. *Nat. Methods* **14**, 1083–1086 (2017).
52. Ginestet, C. ggplot2: elegant graphics for data analysis. *J. R. Stat. Soc. Ser. A* **174**, 245–246 (2011).
53. Kassambara, A. ggpubr: 'ggplot2' based publication ready plots (R package version 0.6.0) https://rpkgs.datanovia.com/ggpubr/ (2023).
54. Hao, Y. et al. Dictionary learning for integrative, multimodal and scalable single-cell analysis. *Nat. Biotechnol.* **42**, 293–304 (2024).
55. McInnes, L. & Healy, J. UMAP: uniform manifold approximation and projection for dimension reduction. Preprint at https://doi.org/10.48550/arXiv.1802.03426 (2018).

Acknowledgements

This study was supported by the National Key Research and Development Program of China (2021YFC2501800) and Shanghai Committee of Science and Technology (20Y11900100, 21MC1930400) to Z.S. and the National Natural Science Foundation of China (82273188), Special Fund for Science and Technology Commission of Shanghai Municipality (20244Z0013) and Clinical Research of Zhongshan Hospital, Fudan University (2020ZSLC07), to D.W. The funding agencies had no role in the preparation of this manuscript. We thank J. Jin (Fudan University) for pMx and LMP backbone plasmids, H. Hu (Sichuan University) for the MIGR1 plasmid, Y. Lu (Shanghai Jiao Tong University) for *Nat10*$^{fl/fl}$ mice, C. Ruan (Fudan University) for aged C57BL/6J mice, C. Duan (Shanghai Jiao Tong University) for technical assistance and L. Ye (Army Medical University) for the LCMV Armstrong virus and P14 mice.

Author contributions

Conceptualization: D.W., Z.S., Z.-L.C., Y.L., H.W. and X.W. Methodology: L.S., Xiaoyan Li, F.X., Z.Y., Y.Y., Xushuo Li, Y.C., T.R., K.W. and Z.H.L. Investigation: L.S., F.X., Y.C., T.R., Z.L. and Z.-L.C. Resources: D.W., Z.S. and Y.L. Writing (original draft): D.W. and L.S. Writing (review and editing): Z.S., Y.L., H.W. and X.W. Project administration: D.W., Z.S., Z.-L.C. and Y.L. Funding: D.W. and Z.S.

Competing interests

The authors declare no competing interests.

Additional information

Extended data is available for this paper at https://doi.org/10.1038/s41590-025-02100-2.

Supplementary information The online version contains supplementary material available at https://doi.org/10.1038/s41590-025-02100-2.

Correspondence and requests for materials should be addressed to Yan Lu, Zhenju Song, Zhou-Li Cheng or Duojiao Wu.

Peer review information *Nature Immunology* thanks María Mittelbrunn and the other, anonymous, reviewer(s) for their contribution to the peer review of this work. Primary Handling Editor: P. Jauregui, in collaboration with the *Nature Immunology* team.

Reprints and permissions information is available at www.nature.com/reprints.

https://doi.org/10.1038/s41590-025-02100-2

a

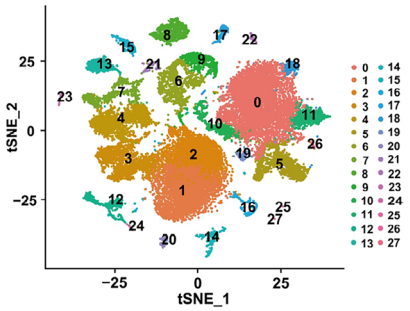

b

	Nat10$^{fl/fl}$-S	*Nat10*$^{fl/fl}$*Cd4*^{Cre}-S
T cells(%)	23.37	5.15
NK cells(%)	3.17	4.51
Monocytes(%)	3.08	5.93
Macrophages(%)	1.89	3.47
Granulocytes(%)	3.65	11.98
Erythrocytes(%)	1.35	0.27
Dendritic cells(%)	0.15	0.12
B cells(%)	63.33	68.57

	Nat10$^{fl/fl}$-T	*Nat10*$^{fl/fl}$*Cd4*^{Cre}-T
T cells(%)	96.09	96.40
NK cells(%)	0.37	0.38
Monocytes(%)	0.10	0.12
Macrophages(%)	0.41	0.47
Granulocytes(%)	0.09	0.28
Erythrocytes(%)	1.65	0.24
Dendritic cells(%)	0.01	0.00
B cells(%)	1.28	2.12

c

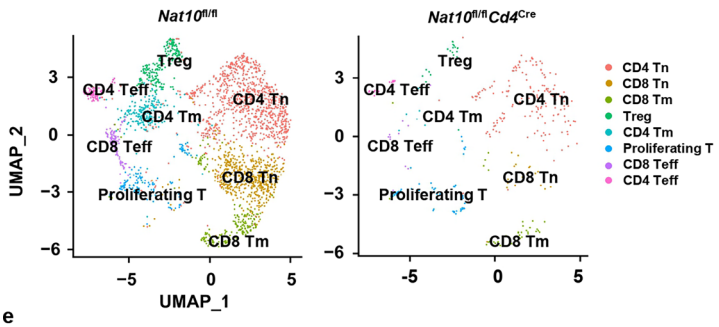

d

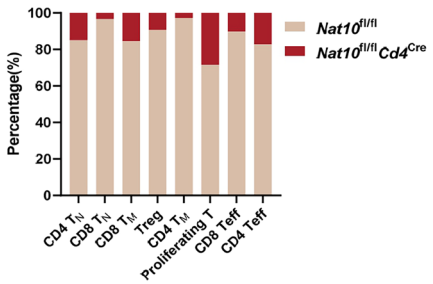

e

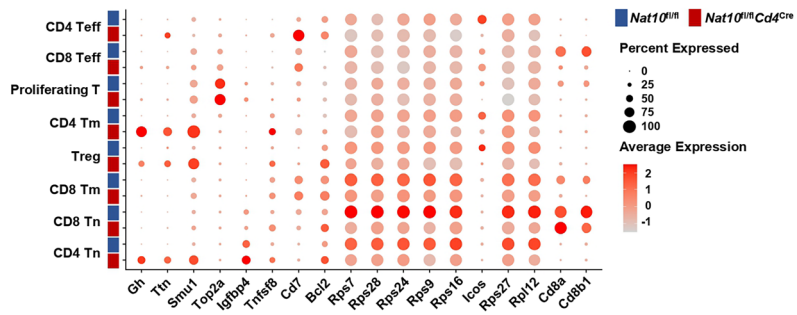

f

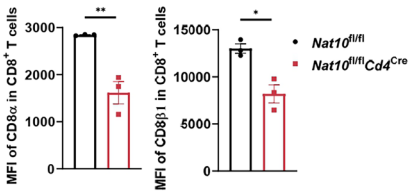

Extended Data Fig. 1 | NAT10 helps to maintain the pool of T cells. a tSNE visualization of splenic and thymic single cells from FLOX and CKO mice by clusters. **b** Table listing the exact percentage of cells from FLOX or CKO mice as a fraction of total T cells for each cluster, corresponding to the bar plot in Fig. 2e. **c** UMAP visualization of splenic T cells from FLOX and CKO mice identified in Fig. 2d. **d** Bar plot showing the percentage of cells from FLOX or CKO mice as a fraction of total T cells for each cluster, related to the UMAP plot in (c). **e** Bubble plot exhibiting the top 8 up-regulated (left) and 10 down-regulated (right) transcripts of CKO versus FLOX splenic T cells. Populations marked by blue and red block represent T cells from FLOX and CKO mice, respectively. **f** Bar graph showing the geometric mean fluorescence intensity (MFI) of CD8α and CD8β1 in FLOX and CKO CD8$^+$T cells. Error bars represent mean ± s.e.m. n = 3 biologically independent samples. **P = 0.0065, *P = 0.0112. Two-tailed, unpaired t-test.

https://doi.org/10.1038/s41590-025-02100-2

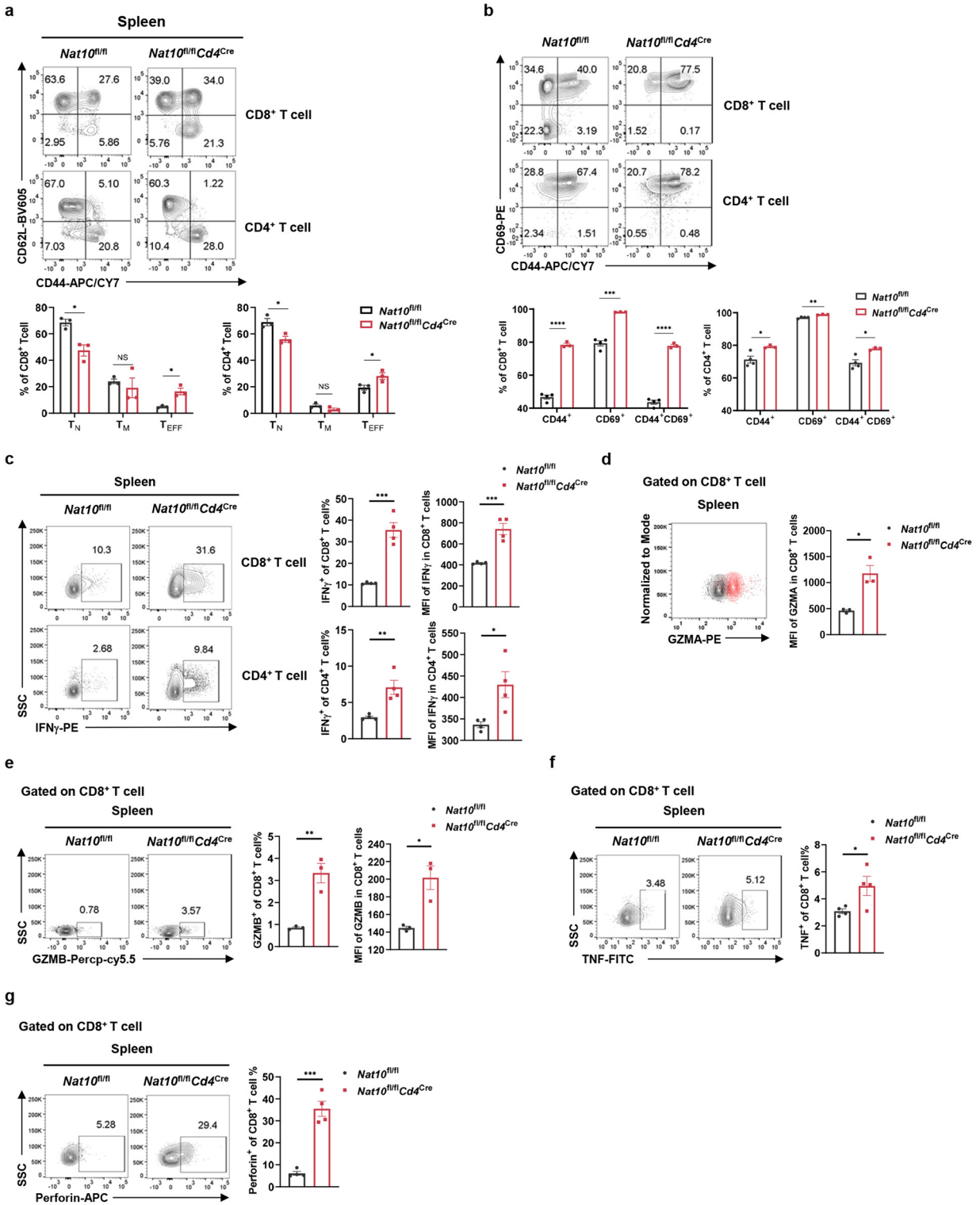

Extended Data Fig. 2 | See next page for caption.

https://doi.org/10.1038/s41590-025-02100-2

Extended Data Fig. 2 | T cell presents hyperactive features after NAT10 deletion. a The fraction of splenic naive ($CD44^{lo}CD62L^{hi}$, T_N), effector ($CD44^{hi}CD62L^{lo}$, T_{EFF}) and memory T cells ($CD44^{hi}CD62L^{hi}$, T_M) were quantified by FCM. Left, representative flow plots. Right, bar graphs showing the percentage of naive, effector, memory T cells in FLOX and CKO mice. n = 3. Exact P values from left to right: *P = 0.0124, *P = 0.0101, *P = 0.0221, *P = 0.0474, NS, P > 0.05. **b** T cell activation measured by CD69 and CD44 staining of activated FLOX and CKO T_N with anti-CD3/28 stimulation for 24 h. Left, representative flow plots. Right, bar plots showing the percentage of $CD44^+$, $CD69^+$ and $CD44^+CD69^+$ T cells in FLOX and CKO $CD8^+$ and $CD4^+$ T cells, respectively. FLOX n = 4, CKO n = 3. Exact P values from left to right: ****P < 0.0001, ***P = 0.0002, *P = 0.0259, **P = 0.0028, *P = 0.0128. **c** Expression of IFNγ in FLOX and CKO T cells measured by FCM. Left, representative flow plots. Right, bar graphs showing $IFNg^+$ fraction as well as IFNγ MFI in FLOX and CKO splenic T cells. n = 4. ***P ($CD8^+$T IFNγ MFI) = 0.0009, ***P ($CD8^+$ $IFN\gamma^+$T%) = 0.0004, **P = 0.0056, *P = 0.024. **d** Expression of GZMA in $CD8^+$ FLOX and CKO T cells measured by FCM. Left, representative flow plots. Right, bar graphs showing $GZMA^+$ fraction and GZMA MFI of $CD8^+$ FLOX and CKO T cells. n = 3. *P = 0.0100. **e** Expression of GZMB in $CD8^+$ FLOX and CKO T cells measured by FCM. Left, representative flow plots. Right, bar graphs showing $GZMB^+$ fraction and GZMB MFI of $CD8^+$ FLOX and CKO T cells. n = 3. **P = 0.0050; *P = 0.0138. **f** Expression of TNF in $CD8^+$ FLOX and CKO T cells measured by FCM. Left, representative flow plots. Right, bar graphs showing TNF^+ fraction and TNF MFI of $CD8^+$ FLOX and CKO T cells. n = 4. *P = 0.0433. **g** Expression of perforin in $CD8^+$ FLOX and CKO T cells measured by FCM. Left, representative flow plots. Right, bar graphs showing the percentage of $perforin^+$ $CD8^+$ FLOX and CKO T cells. n = 4. ***P = 0.0002. The values of "n" all refer to biologically independent samples. Error bars represent mean ± s.e.m. (**a**–**g**). Two-tailed, unpaired t-test (**a**–**g**).

https://doi.org/10.1038/s41590-025-02100-2

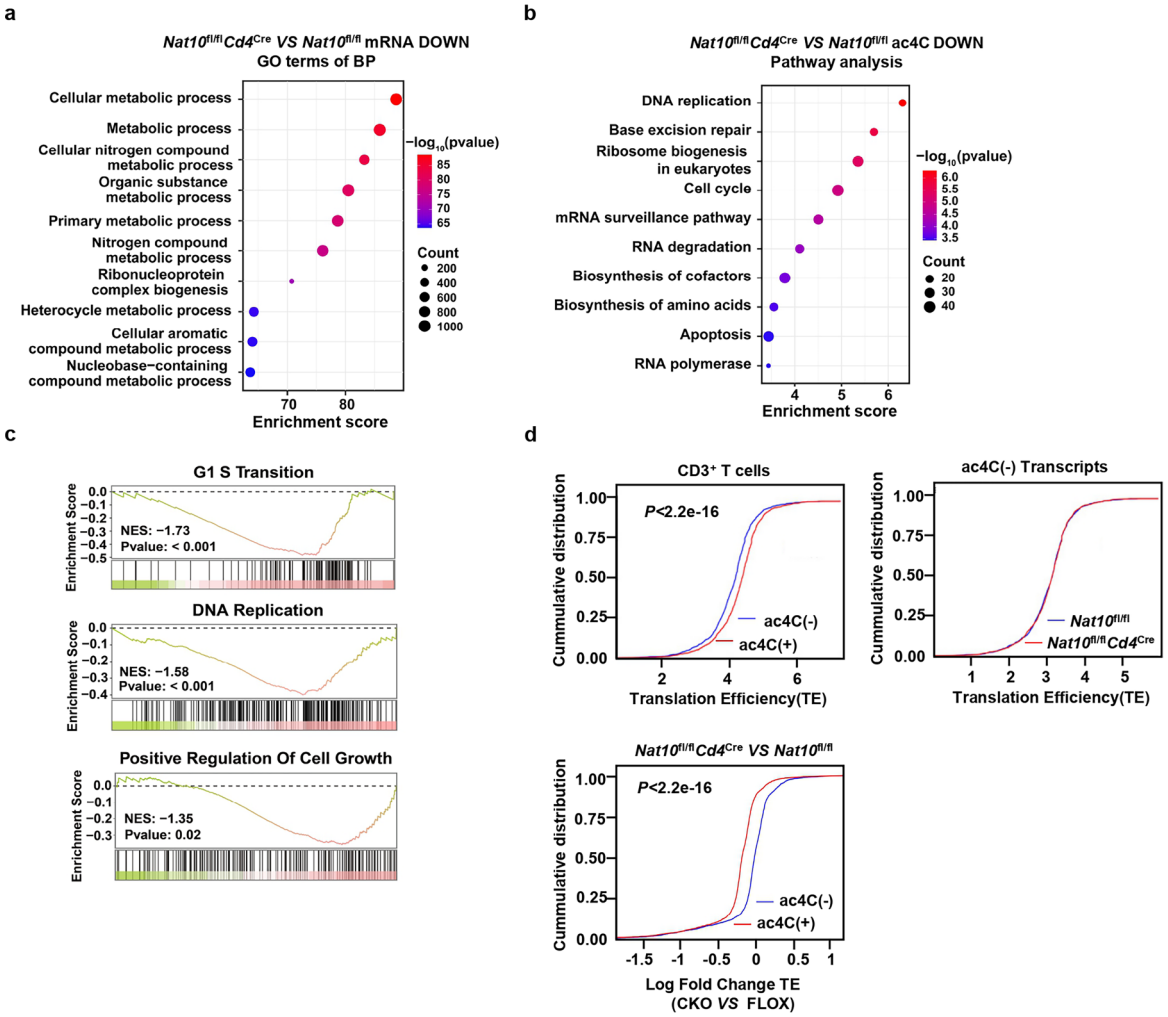

Extended Data Fig. 3 | NAT10 is required for the stability and translation efficiency of *Myc* mRNA. a Gene Ontology (GO) enrichment analysis of down-regulated genes in CKO T cells compared to their FLOX controls. Biological process terms were displayed. **b** KEGG pathway analysis of mRNAs with lower ac4C levels in CKO T cells compared to their FLOX controls. **c** GSEA plots showing significantly enriched gene sets, "DNA replication", "G1 S transition" and "Positive regulation of cell cycle". **d** Cumulative distribution plots of translation efficiency (TE) for ac4C (−)/(+) transcripts in FLOX CD3$^+$ T cells (upper left), and ac4C (−) transcripts in FLOX and CKO T cells (upper right). The cumulative distribution plot of TE relative changes (log fold change, CKO *VS* FLOX) for ac4C (−) and ac4C (+) transcripts was also displayed (down). Hypergeometric test, one-sided, BH adjusted (a, b), two-tailed Kolmogorov–Smirnov test (c) and two-tailed Mann-Whitney U test (d).

https://doi.org/10.1038/s41590-025-02100-2

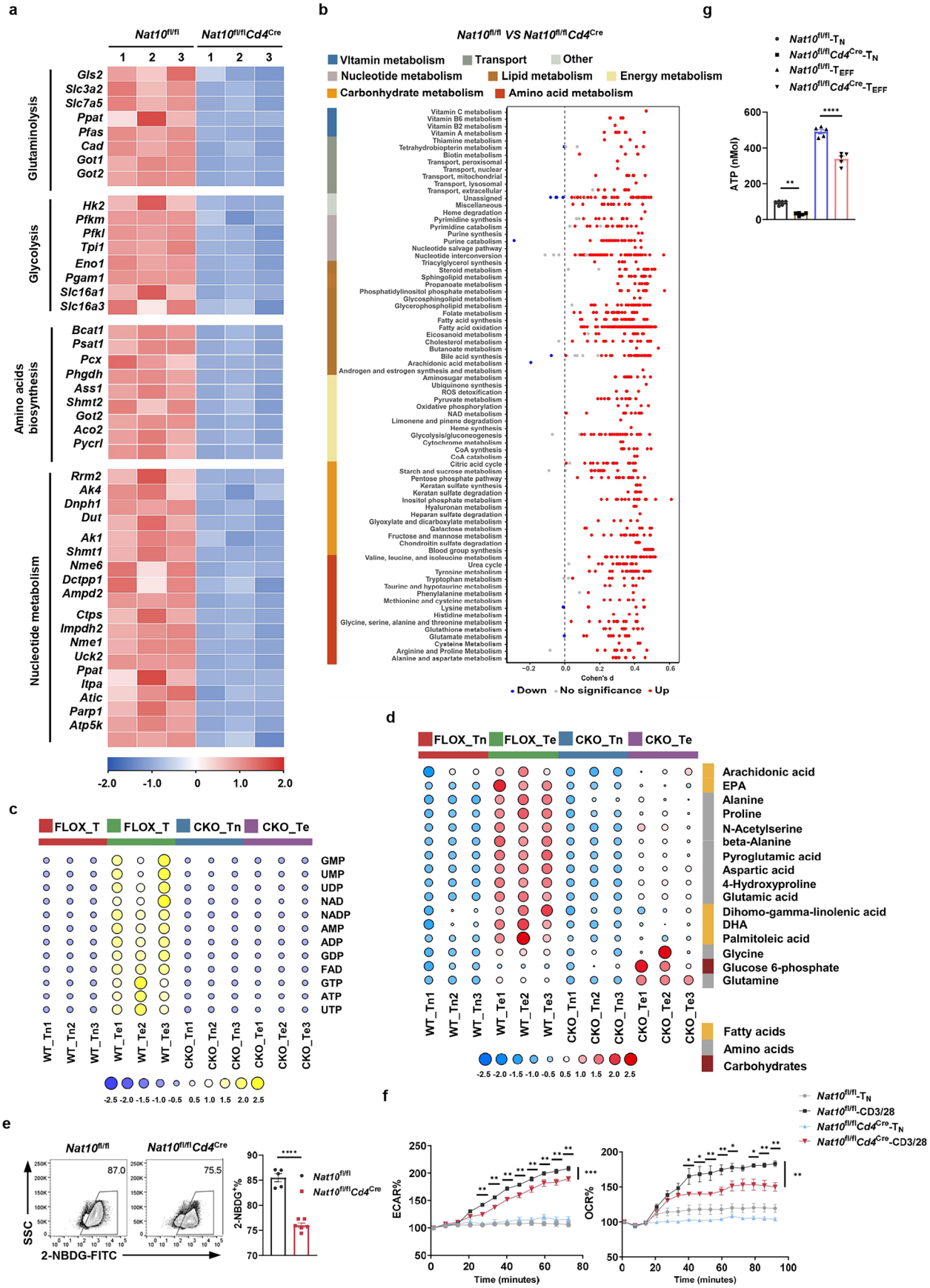

Extended Data Fig. 4 | See next page for caption.

https://doi.org/10.1038/s41590-025-02100-2

Extended Data Fig. 4 | NAT10 deletion causes metabolic dysfunction of T cells. a Heatmap summarizing expressions of critical genes in glutaminolysis, glycolysis, amino acids biosynthesis and nucleotide metabolism in CKO versus FLOX T_{EFF} cells from RNA-seq data (related to Fig. 4a). Expression data was Z-score normalized. **b** Differential activity of indicated metabolic reactions between FLOX and CKO splenic T cells calculated via "Compass" algorithm based on scRNA-seq data. Effect size was assessed with Cohen's d statistic, namely absolute difference in means divided by the pooled SD. **c**, **d** T_N were purified from 8-week-old FLOX and CKO mice, part of which were stimulated with anti-CD3/28 for 24 h. Then, FLOX T_N, CKO T_N as well as their activated counterparts were subjected to metabolic profiling. Heatmap of nucleotide profiles (**c**), metabolite profiles (**d**) in FLOX T_N, FLOX T_{EFF}, CKO T_N and CKO T_{EFF} were presented. Data was Z-score normalized. **e** T_N were purified from 8-week-old FLOX and CKO mice and stimulated with anti-CD3/28 for 24 h. Glucose uptake measured by 2-NBDG fluorescence intensity through FCM was displayed. FLOX n = 5, CKO n = 6. ****P < 0.0001. **f** Relative ECAR and OCR of FLOX and CKO T_N measured at baseline or with anti-CD3/CD28 beads stimulation. For ECAR, FLOX-T_N n = 10, CKO-T_N n = 9, FLOX-CD3/28 n = 7, CKO-CD3/28 n = 8; ***P (interaction) = 0.0006, P (*marked timepoint) = 0.0092, 0.0081, 0.0022, 0.0043, 0.0051, 0.0096, 0.0020, 0.0043, respectively. For OCR, FLOX-T_N n = 9, CKO-T_N n = 3, FLOX-CD3/28 n = 5, CKO-CD3/28 n = 4; **P (interaction) = 0.0090, P (*marked timepoint) = 0.0422, 0.0135, 0.0070, 0.0056, 0.0270, 0.0193, 0.0098, 0.0017, respectively. **g** T_N were purified from 8-week-old FLOX and CKO mice, part of which were stimulated with anti-CD3/28 for 24 h. Then, ATP production of FLOX-T_N (n = 6), CKO-T_N (n = 5) as well as their activated counterparts (n = 5) were measured. **P = 0.0016, ****P < 0.0001. The values of "n" all refer to biologically independent samples. Error bars represent mean ± s.e.m. (**e**–**g**). Two tailed, negative binomial distribution test (**e**); two-tailed, two-way ANOVA with Šídák's multiple comparisons test (**f**); two-tailed, one-way ANOVA with Tukey's multiple comparisons test (**g**).

https://doi.org/10.1038/s41590-025-02100-2

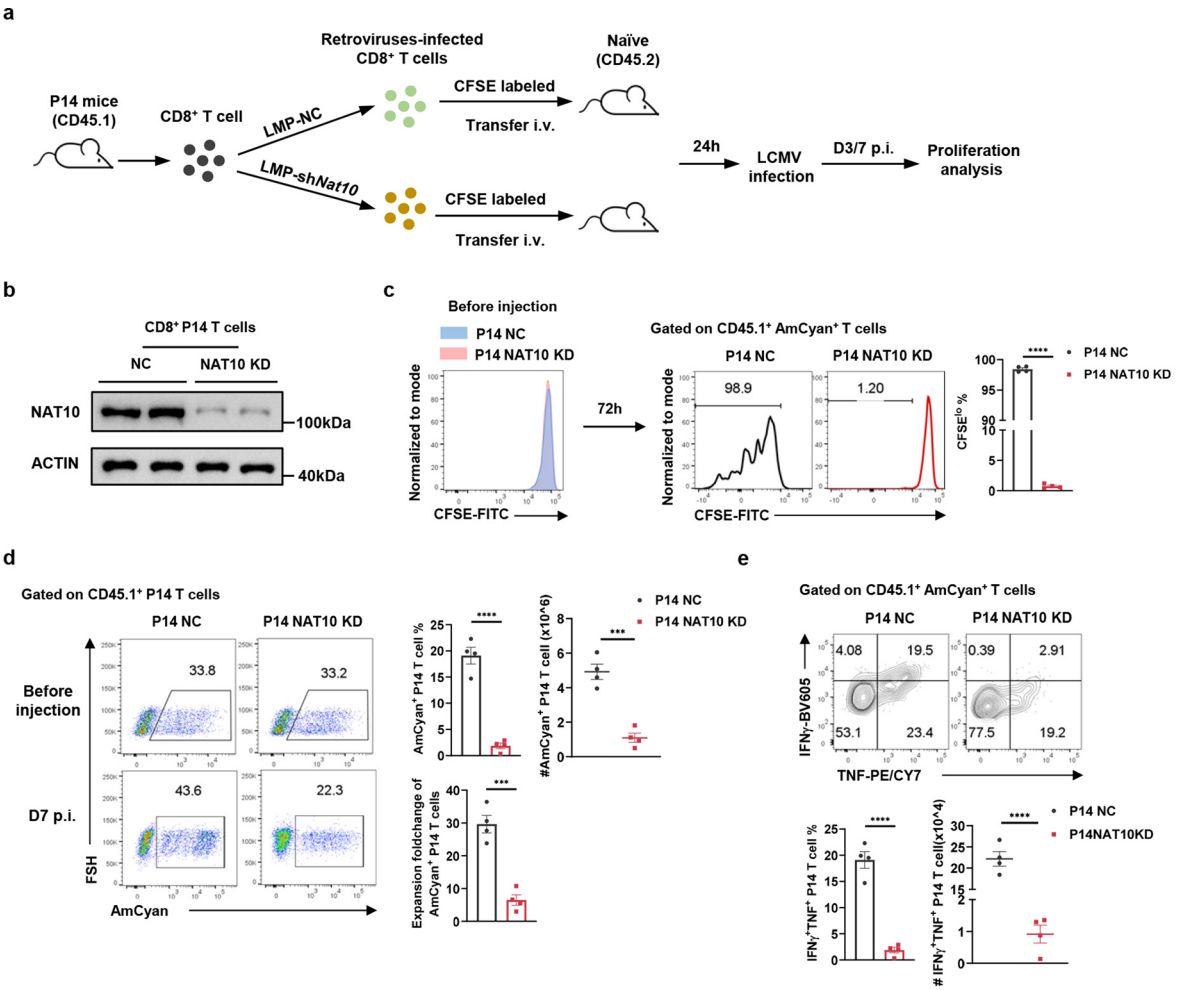

Extended Data Fig. 5 | NAT10 knockdown compromised proliferative potency of P14 T cells in response to LCMV infection. a Schematic diagram of in vivo experiments to explore the role of NAT10 in specific-antiviral response of P14 T cells. CD45.1$^+$ CD8$^+$ P14 T cells were isolated, labeled with CFSE, and then infected by retrovirus containing LMP-NC and LMP-*Nat10*-shRNA plasmids, respectively. Equal amounts of these T cells (4×10^5 cells) were then i.v. injected into 8-week-old CD45.2$^+$ recipient mice 1 day before *Armstrong* infection. 3 or 7 days later, the recipients were sacrificed for proliferation analysis. **b** Knockdown efficiency of NAT10 was assessed by western blot analysis. Representative data of three independent experiments is presented. **c** CFSE dilution analysis before injection and 72 h after LCMV infection. Left, representative flow plots. Right, bar graphs showing percentages of CFSE^{lo} P14 T cells in the 2 groups, respectively. n = 4, ****P < 0.0001. **d** Proportion of retrovirally infected P14 T cells identified by AmCyan fluorescence. Left, representative flow plots. Right, bar diagrams showing the percentage, absolute number and expansion folds of AmCyan$^+$ P14 T cells in each group. n = 4, ****P < 0.0001, ***P (#AmCyan$^+$ P14 T cell) = 0.0003, ***P (Expansion foldchange) = 0.0003. **e** Detection of IFNγ$^+$ TNF$^+$ AmCyan$^+$ P14 T cells in recipients with control or NAT10 KD P14 T cells adaptive transfer, respectively. Up, representative flow plots. Down, bar diagrams exhibiting percentages and absolute number of splenic IFNγ$^+$ TNF$^+$ AmCyan$^+$ P14 T cells in the two groups. n = 4. ****P < 0.0001. The values of "n" all refer to biologically independent samples. Error bars represent mean ± s.e.m. (**c**–**e**). Two-tailed, unpaired t-test (**c**–**e**).

https://doi.org/10.1038/s41590-025-02100-2

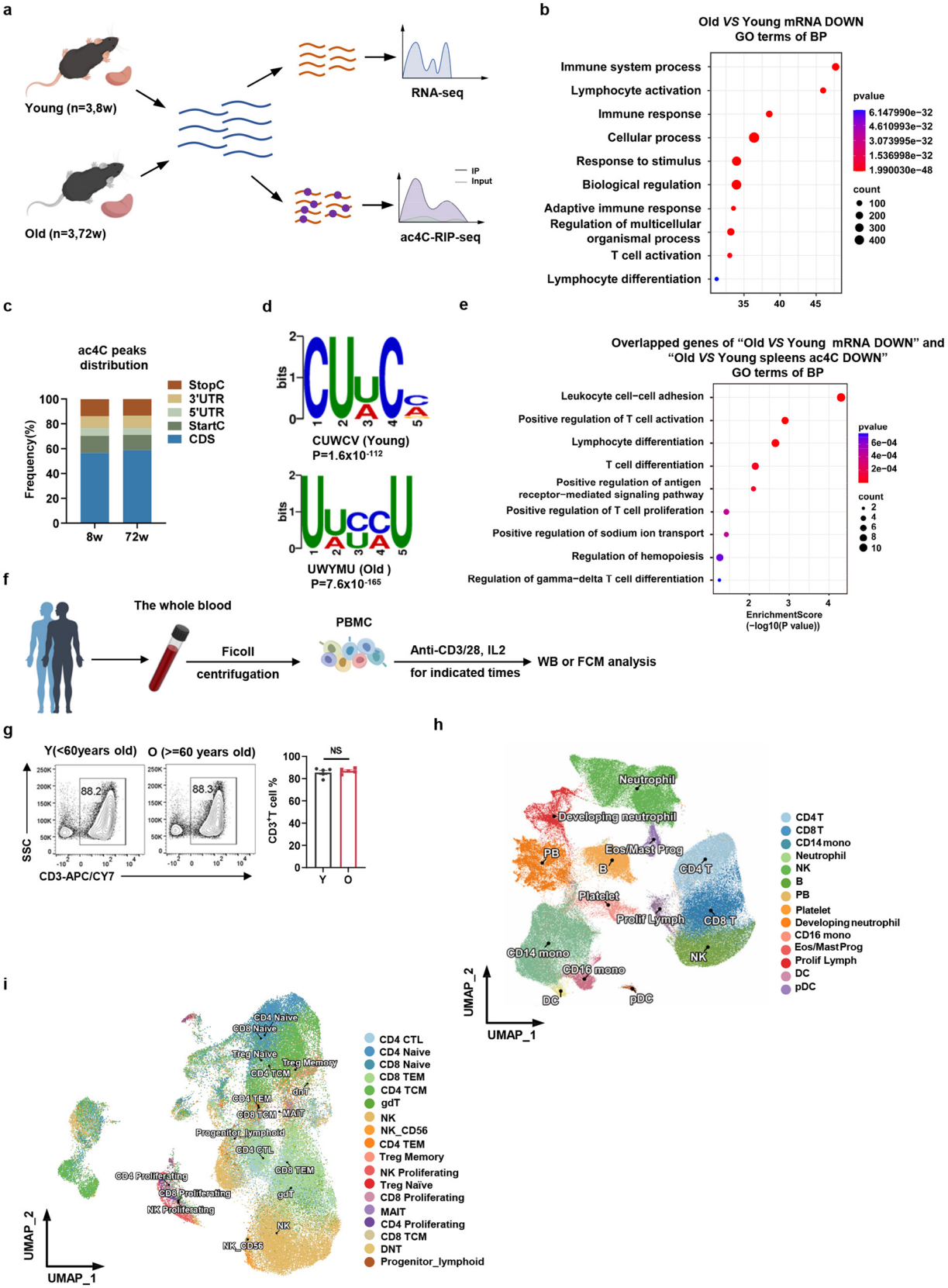

Extended Data Fig. 6 | See next page for caption.

https://doi.org/10.1038/s41590-025-02100-2

Extended Data Fig. 6 | Exploration of reduced NAT10 levels in immune senescence. a Schematic diagram of RNA-seq and ac4C-RIP-seq performed on spleen from young (8w) and aged (72w) mice. **b** GO enrichment analysis of transcripts with less ac4C modification in splenocytes from old mice compared to their young controls. Biological process terms were displayed. **c** Bar graph showing ac4C peak distribution on mRNAs of splenocytes from young (8w) and old (72w) mouse. **d** Motif analysis for ac4C peaks in spleen from young (8w) and old (72w) mice. **e** GO enrichment analysis of the overlapped genes between "Old *VS* Young mRNA down" (n = 679) and "Old *VS* Young ac4C down" (n = 1586) genes. Biological process terms were displayed. **f** Schematic diagram showing isolation and culture procedure of PBMC. **g** Percentages of $CD3^+$ T cells in PBMC from young (<60 years old) and old (≥60 years old) subjects with anti-CD3/28 stimulation for 48 h. Left, representative flow plots. Right, bar graph displaying the percentage of $CD3^+$T cells after 48h-culture (n = 5 biologically independent samples.). Error bars represent mean ± s.e.m., NS $P > 0.05$ by two-tailed, unpaired t-test. **h** UMAP visualization of PBMC from 33 COVID-19 patients and 8 healthy controls according to scRNA-seq data from Wilk, Aaron J et al.[22]. **i** Deeper UMAP visualization of NK and T cells identified in (**h**). Hypergeometric test, one-sided, BH adjusted (**b, d, e**). Icons in Extended Data Fig. 6a, f were from Figdraw (https://www.figdraw.com/) with the agreement ID: RIARO787e2.

https://doi.org/10.1038/s41590-025-02100-2

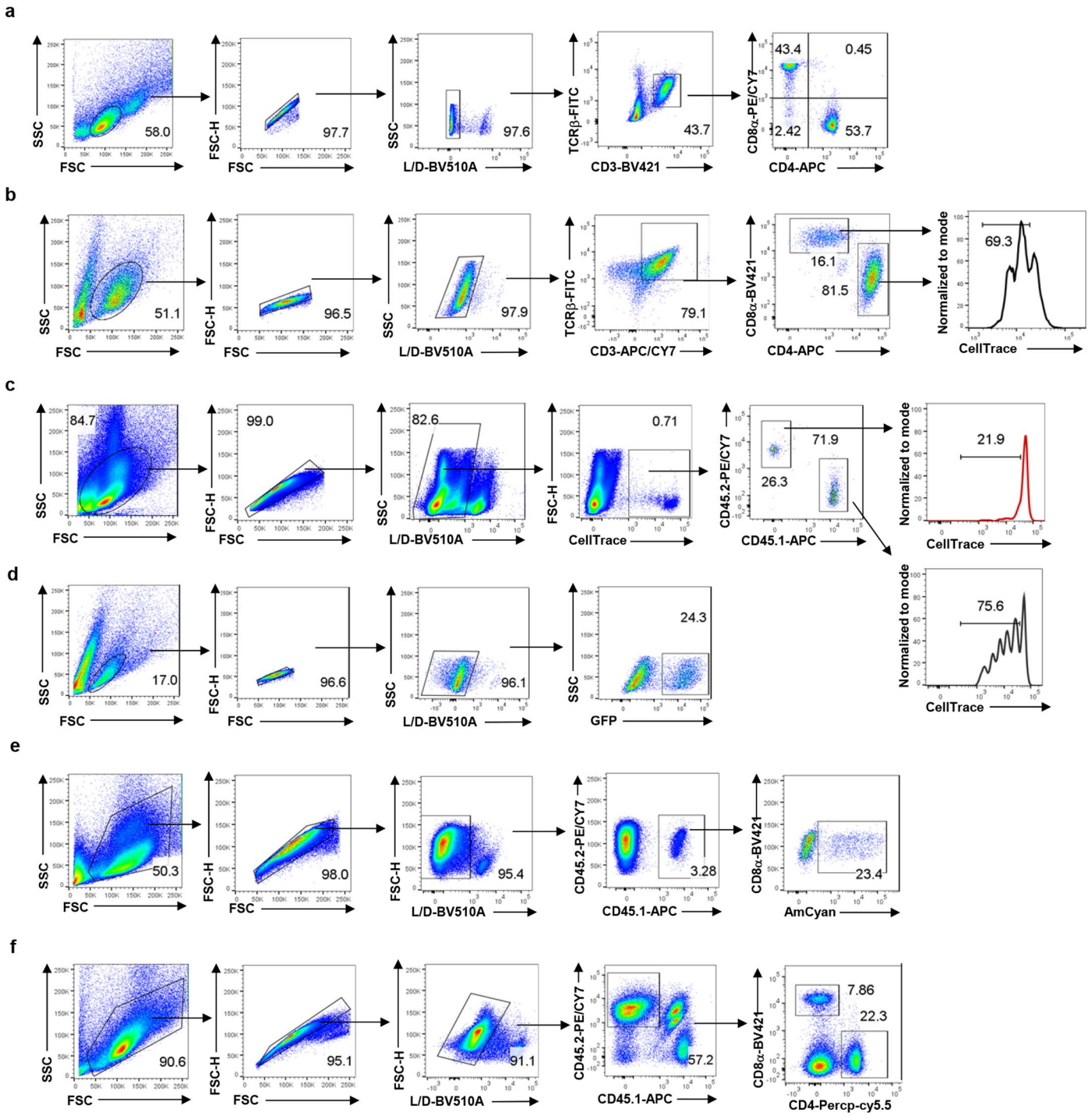

Extended Data Fig. 7 | Gating strategies. Representative flow cytometry gating strategies for main T cell subsets (**a**), in vitro (**b**) and in vivo (**c**) CellTrace or CFSE dilution in T cells. Gating strategies used for identifying T cells with plasmids successfully transformed were displayed in (**d**) and (**e**). T cells deriving from transferred HSCs in chemic mice were showed in (**f**).

nature portfolio

Corresponding author(s): Duojiao Wu

Last updated by author(s): Nov 12, 2024

Reporting Summary

Nature Portfolio wishes to improve the reproducibility of the work that we publish. This form provides structure for consistency and transparency in reporting. For further information on Nature Portfolio policies, see our Editorial Policies and the Editorial Policy Checklist.

Statistics

For all statistical analyses, confirm that the following items are present in the figure legend, table legend, main text, or Methods section.

n/a	Confirmed
☐	☒ The exact sample size (*n*) for each experimental group/condition, given as a discrete number and unit of measurement
☐	☒ A statement on whether measurements were taken from distinct samples or whether the same sample was measured repeatedly
☐	☒ The statistical test(s) used AND whether they are one- or two-sided *Only common tests should be described solely by name; describe more complex techniques in the Methods section.*
☐	☒ A description of all covariates tested
☐	☒ A description of any assumptions or corrections, such as tests of normality and adjustment for multiple comparisons
☐	☒ A full description of the statistical parameters including central tendency (e.g. means) or other basic estimates (e.g. regression coefficient) AND variation (e.g. standard deviation) or associated estimates of uncertainty (e.g. confidence intervals)
☐	☒ For null hypothesis testing, the test statistic (e.g. *F*, *t*, *r*) with confidence intervals, effect sizes, degrees of freedom and *P* value noted *Give P values as exact values whenever suitable.*
☒	☐ For Bayesian analysis, information on the choice of priors and Markov chain Monte Carlo settings
☒	☐ For hierarchical and complex designs, identification of the appropriate level for tests and full reporting of outcomes
☐	☒ Estimates of effect sizes (e.g. Cohen's *d*, Pearson's *r*), indicating how they were calculated

Our web collection on statistics for biologists contains articles on many of the points above.

Software and code

Policy information about availability of computer code

Data collection

1.RNA-/acRIP-/Ribo-/scRNA-seq data were sequenced by the Illumina NovaSeq 6000 platform.
2.Ultra-high-performance liquid chromatography tandem mass spectrometry (UPLC-MS/MS) data were collected with AB Sciex QTRAP 6500 LC-MS/MS system.
3.RT-qPCR data were collected with Applied Biosystems™ 7500 Systerm.
4.Immunoblots were collected with ChemiScope 6100 Imaging System.
5.Flow cytometry data were collected with BD FACSLyric™ Flow Cytometry System.
6.Metabolic flux data were collected from XF-96 Extracellular Flux Analyzer (Seahorse Bioscience).

Data analysis	1.For flow cytometry, Flowjo (v 10.4) was used. Numerical data were exported to Excel (16.54) and analyzed by Graphpad Prism (v.9.0.0). 2.For RNA-seq and acRIP-seq, paired-end clean reads of all libraries were aligned to the reference genome (MM10) by Hisat2 software (v2.0.4). Then, HTSeq software (v0.9.1) was used to get the raw count, and edgeR was used to perform normalization. For acRIP-seq, clean reads were aligned to the reference genome (MM10) by Hisat2 software (v2.0.4). Acetylated sites on RNAs (peaks) were identified by MACS software. Differentially acetylated sites were identified by diffReps. For ribo-seq, the rRNA and tRNA-removed reads of each sample were mapped to the reference genome by Tophat2. For scRNA-seq, raw sequencing reads were quality-controlled and annotated through the BD Rhapsody Whole Transcriptome Assay Analysis Pipeline (v1.8). Genome Reference Consortium Human Build 38 (GRCh38) was used as reference. 3.Graphpad prism (v.9.0.0) and Excel (16.54) were used to analyze the RT-qPCR data. 4.For immunoblotting, the densitometry analysis was performed via ImageJ v.1.53a software. 5.Integrative Genomics Viewer (IGV, v2.4.10) was used to visualize the acRIP- or ChIP-seq data.

For manuscripts utilizing custom algorithms or software that are central to the research but not yet described in published literature, software must be made available to editors and reviewers. We strongly encourage code deposition in a community repository (e.g. GitHub). See the Nature Portfolio guidelines for submitting code & software for further information.

Data

Policy information about availability of data

All manuscripts must include a data availability statement. This statement should provide the following information, where applicable:

- Accession codes, unique identifiers, or web links for publicly available datasets
- A description of any restrictions on data availability
- For clinical datasets or third party data, please ensure that the statement adheres to our policy

The bulk RNA and acRIP sequencing data in this study were deposited in the Genome Sequence Archive (GSA) with the accession ID CRA015058, CRA015065, CRA015132 and CRA015079. scRNA-seq data were uploaded to the GSA with the accession ID CRA015122. The ChIP sequencing data are accessible from Gene Expression Omnibus database (GEO) with the following accession IDs: GSE99319, GSE64409, GSE54191, and GSE40918. Metabolomics raw data in this study were deposited in the MetaboLights database with the accession ID MTBLS9639 and MTBLS9640. Quantitative information of metabolites detected was displayed in supplementary table 2-3. Processed scRNA-seq data of COVID-19 patients provided by Blish lab could be acquired from the COVID-19 Cell Atlas (https://www.covid19cellatlas.org/). RNA-seq data of leucocytes from COVID-19 patients were available from GEO with the accession ID GSE157103.

Research involving human participants, their data, or biological material

Policy information about studies with human participants or human data. See also policy information about sex, gender (identity/presentation), and sexual orientation and race, ethnicity and racism.

Reporting on sex and gender	Sex was not considered as an inclusion criterion in this study. In western blot experiment detecting NAT10 expression, both the "Young" and "Old" group included 3 men and 2 women.
Reporting on race, ethnicity, or other socially relevant groupings	There were no differences in race, ethnicity or other socially relevant groupings among the healthy donors.
Population characteristics	In this study, all PBMC samples were collected from healthy donors, who were defined as follows: a) aged 18 – 85 years old; b) absence of infectious diseases over the past 6 months; c) without malignant tumor history; and d) without autoimmune diseases history. Blood routine examination was performed to ensure the quality and eligibility of each donor. A total of 10 samples were collected, with 2-3ml whole blood for each. These subjects were grouped into "Young" and "Old" based on whether they were younger or older than 60 years old..
Recruitment	All of the subjects were recruited in Jinshan Hospital, Shanghai with written informed consent.
Ethics oversight	The study was approved by the Ethics Committee of Jinshan Hospital (JIEC 2023-S47).

Note that full information on the approval of the study protocol must also be provided in the manuscript.

Field-specific reporting

Please select the one below that is the best fit for your research. If you are not sure, read the appropriate sections before making your selection.

☒ Life sciences ☐ Behavioural & social sciences ☐ Ecological, evolutionary & environmental sciences

For a reference copy of the document with all sections, see nature.com/documents/nr-reporting-summary-flat.pdf

Life sciences study design

All studies must disclose on these points even when the disclosure is negative.

Sample size	No sample size calculations were performed. But sample sizes in this study are similar to those published in previous researches.

Data exclusions	2 samples in CKO group were removed from the bar graph comparing percentages of KRG1loCD127hi GP33+ CD8+ T cells because the collected GP33+ CD8+ T cells were too few (cell number <400) to reflect the accurate biological features (FIG 7K). For patient samples from GSE157103, 3 patients were removed for missing age data. One patient sample was excluded as an outlier (with NAT10 and MYC expression value outside the mean±2.5SD).No other data were excluded.
Replication	The number of biological replicates and independent experiments were stated in the figure legend.
Randomization	Mice were grouped by genotype or age and PBMC samples were grouped according to donors' ages, thus not randomized.
Blinding	Virus injection and measurement of seral virus copies were performed in a blinded manner.

Reporting for specific materials, systems and methods

We require information from authors about some types of materials, experimental systems and methods used in many studies. Here, indicate whether each material, system or method listed is relevant to your study. If you are not sure if a list item applies to your research, read the appropriate section before selecting a response.

Materials & experimental systems

n/a	Involved in the study
☐	☒ Antibodies
☐	☒ Eukaryotic cell lines
☒	☐ Palaeontology and archaeology
☐	☒ Animals and other organisms
☒	☐ Clinical data
☒	☐ Dual use research of concern
☒	☐ Plants

Methods

n/a	Involved in the study
☒	☐ ChIP-seq
☐	☒ Flow cytometry
☒	☐ MRI-based neuroimaging

Antibodies

Antibodies used

Rabbit anti NAT10 Abcam Cat# ab194297 1:2000
Mouse anti Beta actin Proteintech Cat# 66009-1-Ig;
RRID: AB_2687938 1:5000
Ultra-LEAF™ Purified anti-mouse CD3ε Biolegend Cat# 100371;
RRID: AB_2616674 5ug/ml
Ultra-LEAF™ Purified anti-mouse CD28 Biolegend Cat# 102122;
RRID: AB_11147170 0.5ug/ml
Rabbit anti-N4-acetylcytidine (ac4C) Abcam Cat# ab252215;
RRID: AB_2827750 1:1000
CDC25A Polyclonal antibody Proteintech Cat# 55031-1-AP 1:1000
Recombinant Anti-Cdk2 antibody [E304] Abcam Cat# ab32147
RRID: AB_726775 1:2000
Recombinant Anti-Cdk4 antibody [EPR17525] Abcam Cat# ab199728
RRID: AB_2920615 1:2000
Recombinant Anti-c-Myc antibody [Y69] Abcam Cat# ab32072
RRID: AB_731658 1:1000
HRP-conjugated Affinipure Goat Anti-Rabbit IgG(H+L) Proteintech Cat# SA00001-2
RRID: AB_2722564 1:5000
HRP-conjugated Affinipure Goat Anti-Mouse IgG(H+L) Proteintech Cat# SA00001-1
RRID: AB_2722565 1:5000
APC-Cy™7 Hamster Anti-Mouse CD3e (145-2C11) BD Pharmingen Cat# 557596
RRID: AB_396759 1:200
APC anti-mouse CD3e (145-2C11)BD Pharmingen Cat# 553066
RRID: AB_398529 1:200
BV421 anti-mouse CD3e (145-2C11) BD Pharmingen Cat# 562600
RRID: AB_11153670 1:200
APC anti-mouse CD4 (RM4-5) Biolegend Cat# 100516
RRID: AB_312718 1:200
PerCP-Cy™5.5 Rat Anti-Mouse CD4 (RM4-5) BD Pharmingen Cat# 550954
RRID: AB_393977 1:200
Brilliant Violet 421™ anti-mouse CD8a (53-6.7) Biolegend Cat# 100737
RRID: AB_10897101 1:200
PE-Cy™7 Rat Anti-Mouse CD8a (53-6.7) BD Pharmingen Cat# 552877
RRID: AB_394506 1:200
Brilliant Violet 605™ anti-mouse IFN-γ (XMG1.2) Biolegend Cat# 505840
RRID: AB_2734493 1:100
FITC anti-mouse TNF-alpha (MP6-XT22) Biolegend Cat# 506304
RRID: AB_315425 1:200

FITC anti-mouse Ki67 (B56) BD Pharmingen Cat# 563462
RRID: AB_2738221 1:100
FITC anti-mouse TCR β chain (H57-597) Biolegend Cat# 109206
RRID: AB_313428 1:200
Brilliant Violet 605™ anti-mouse TCR β chain (H57-597) Biolegend Cat# 109241
RRID: AB_2629563 1:200
Brilliant Violet 421™ anti-mouse CD8b (YTS156.7.7) Biolegend Cat# 126629
RRID: AB_2800620 1:200
Brilliant Violet 605™ anti-mouse CD62L (MEL-14) Biolegend Cat# 104438
RRID: AB_2563058 1:200
PE anti-mouse CD69 (H1.2F3) Biolegend Cat# 104507
RRID: AB_313110 1:200
PE Rat Anti-Mouse IFN-γ (XMG1.2) BD Pharmingen Cat# 554412
RRID: AB_395376 1:100
PE anti-mouse Granzyme A (3G8.5) Biolegend Cat# 149704
RRID: AB_2565309 1:100
APC anti-mouse Perforin (S16009B) Biolegend Cat# 154403
RRID: AB_2721465 1:100
PerCP/Cyanine5.5 anti-human/mouse Granzyme B Recombinant Antibody (QA16A02) Biolegend Cat# 372212 RRID: AB_2728379
1:100
PerCP/Cyanine5.5 anti-mouse CD45 (30-F11)Biolegend Cat# 103131
RRID: AB_893344 1:200
PE anti-human CD3 (HIT3a) Biolegend Cat# 300308
RRID: AB_314044 1:200
Brilliant Violet 421™ anti-human CD3 (OKT3) Biolegend Cat# 317343
RRID: AB_2565848 1:200
PE-Cy™7 Mouse Anti-Human CD69 (FN50) BD Pharmingen Cat# 560712
RRID: AB_1727509 1:200
APC/Cyanine7 anti-human CD3 (OKT3) Biolegend Cat# 317342
RRID: AB_2563409 1:200
Alexa Fluor® 700 Mouse Anti-Human CD8 (RPA-T8) BD Pharmingen
Cat# 557945 RRID: AB_396953 1:200
BV421 Mouse Anti-Human CD25 (2A3) BD Horizon Cat# 564033
RRID: AB_2738555 1:200
BV605 Mouse Anti-Human CD4 (RPA-T4) BD Horizon Cat# 562658
RRID: AB_2744420 1:200
T-Select H-2Db LCMV gp33 (C9M) Tetramer-KAVYNFATM-PE
MBL Life science Cat# TS-M512-1 1:25
APC/Cyanine7 anti-mouse/human CD44 (IM7) Biolegend Cat# 103028
RRID: AB_830784 1:200

Validation

All of the antibodies have been validated by the manufacturers. Validation data are available on product datasheet and published literature.

Eukaryotic cell lines

Policy information about cell lines and Sex and Gender in Research

Cell line source(s)	Plat E. cell line was a gift from Professor Jun Jin. HEK-293T cells were from ATCC.
Authentication	No cell lines in this study were authenticated.
Mycoplasma contamination	All cell lines used were tested negative for Mycoplasma contaminatiom.
Commonly misidentified lines (See ICLAC register)	No commonly misidentified lines were used.

Animals and other research organisms

Policy information about studies involving animals; ARRIVE guidelines recommended for reporting animal research, and Sex and Gender in Research

Laboratory animals	6-8 week old C57BL/6J WT mice were purchased from SPF (Beijing) biotechnology co., LTD. 72 week old C57BL/6J mice were purchased from Jiangsu Huachuang sino Pharma Tech Co.,Ltd. P14 mice were gifted from Professor Lilin Ye.Nat10flox/flox mice were gifted from Professor Yan Lu. Cd4Cre mice were purchased from Cyagen Biosciences Corporation. To generate Nat10 conditional knockout mice, Nat10flox/flox mice were crossed with Cd4Cre mice. Rag2-/- mice were purchased from Cyagen Biosciences Corporation. Mice were routinely housed and handled in Cyagen Biosciences Corporation and Shanghai Public Health Clinical Center under SPF conditions following institutional guidelines.
Wild animals	No wild animals were used in this study.
Reporting on sex	Male and female mice were both used in this study and sex-matched controls were applied throughout the study. According to our

Reporting on sex	preliminary experiment, Nat10 loss resulted in similar T cell contraction and antiviral deficiency in male and female mice. Therefore, the sex information was not collected and disaggregated in the data shown for the manuscript.
Field-collected samples	No field-collected samples were used in this study.
Ethics oversight	Animal procedures were reviewed and approved by the Institutional Animal Care and Use Committee (IACUC) of Shanghai Public Health Clinical Center(2023-A053-01).

Note that full information on the approval of the study protocol must also be provided in the manuscript.

Plants

Seed stocks	*Report on the source of all seed stocks or other plant material used. If applicable, state the seed stock centre and catalogue number. If plant specimens were collected from the field, describe the collection location, date and sampling procedures.*
Novel plant genotypes	*Describe the methods by which all novel plant genotypes were produced. This includes those generated by transgenic approaches, gene editing, chemical/radiation-based mutagenesis and hybridization. For transgenic lines, describe the transformation method, the number of independent lines analyzed and the generation upon which experiments were performed. For gene-edited lines, describe the editor used, the endogenous sequence targeted for editing, the targeting guide RNA sequence (if applicable) and how the editor was applied.*
Authentication	*Describe any authentication procedures for each seed stock used or novel genotype generated. Describe any experiments used to assess the effect of a mutation and, where applicable, how potential secondary effects (e.g. second site T-DNA insertions, mosiacism, off-target gene editing) were examined.*

Flow Cytometry

Plots

Confirm that:

☒ The axis labels state the marker and fluorochrome used (e.g. CD4-FITC).

☒ The axis scales are clearly visible. Include numbers along axes only for bottom left plot of group (a 'group' is an analysis of identical markers).

☒ All plots are contour plots with outliers or pseudocolor plots.

☒ A numerical value for number of cells or percentage (with statistics) is provided.

Methodology

Sample preparation	Spleen, thymus, lymph nodes, lung, kidney and liver were collected and ground through 70um filters. Erythrocytes were lysed with red blood cell lysis buffer and remaining cells were isolated by centrifugation. Primary T cells isolated from spleens were cultured with CD3/28 stimulation in the presence of IL2 to generate activated T cells.
Instrument	Flow cytometry data were collected with BD FACSLyric™ Flow Cytometry System. Flow sorting was performed using BD FACSAria™ III
Software	Flowjo (v 10.4) was used for flow data analysis.
Cell population abundance	20,000-100,000 live cells were acquired and analyzed for each independent experiment.
Gating strategy	Cells were first gated on FSC/SSC to exclude debris, and then on FSC/FSH to remove doublets. Dead cells were excluded via BD Horizon™ Fixable Viability Stain 510 and the live ones were further analyzed.

☒ Tick this box to confirm that a figure exemplifying the gating strategy is provided in the Supplementary Information.